



# Anomaly in the Opacity of the Post-reionization Intergalactic Medium in the Ly $\alpha$ and Ly $\beta$ Forest

Anna-Christina Eilers<sup>1,2</sup> , Joseph F. Hennawi<sup>1,3</sup> , Frederick B. Davies<sup>3</sup> , and Jose Oñorbe<sup>4</sup>

<sup>1</sup>Max-Planck-Institute for Astronomy, Königstuhl 17, D-69117 Heidelberg, Germany; [eilers@mpia.de](mailto:eilers@mpia.de)

<sup>2</sup>International Max Planck Research School for Astronomy & Cosmic Physics at the University of Heidelberg, Germany

<sup>3</sup>Physics Department, University of California, Santa Barbara, CA 93106-9530, USA

<sup>4</sup>Institute for Astronomy, University of Edinburgh, Blackford Hill, EH9 3HJ, Edinburgh, UK

Received 2019 April 3; revised 2019 June 12; accepted 2019 June 18; published 2019 August 8

## Abstract

We measure the intergalactic medium (IGM) opacity in the Ly $\alpha$  as well as in the Ly $\beta$  forest along 19 quasar sightlines between  $5.5 \lesssim z_{\text{abs}} \lesssim 6.1$ , probing the end stages of the reionization epoch. Owing to its lower oscillator strength, the Ly $\beta$  transition is sensitive to different gas temperatures and densities than Ly $\alpha$ , providing additional constraints on the ionization and thermal state of the IGM. A comparison of our measurements to different inhomogeneous reionization models, derived from post-processing the Nyx cosmological hydrodynamical simulation to include spatial fluctuations in the ultraviolet background or the gas temperature field, as well as to a uniform reionization model with varying thermal states of the IGM, leads to two primary conclusions: First, we find that including the effects of spectral noise is key for a proper data to model comparison. Noise effectively reduces the sensitivity to high-opacity regions, and thus even stronger spatial inhomogeneities are required to match the observed scatter in the observations than previously inferred. Second, we find that models that come close to reproducing the distribution of Ly $\alpha$  effective optical depths nevertheless underpredict the Ly $\beta$  opacity at the same spatial locations. The origin of this disagreement is not entirely clear, but models with an inversion in the temperature–density relation of the IGM just after reionization is completed match our measurements best, although they still do not fully capture the observations at  $z \gtrsim 5.8$ .

**Key words:** dark ages, reionization, first stars – intergalactic medium – methods: data analysis – quasars: absorption lines

## 1. Introduction

The first billion years of our universe are at the forefront of observational and theoretical cosmological research. During this early evolutionary epoch, the intergalactic medium (IGM) transitioned from a neutral state following recombination to a highly ionized state due to the radiation emitted by the first stars, galaxies, and quasars. However, despite significant progress in recent years, the details of this reionization process, such as its precise timing and morphology, remain unclear.

The absorption features of neutral hydrogen within the IGM imprinted on quasar sightlines at  $z \gtrsim 6$  have proven to be a valuable observational tool to constrain the Epoch of Reionization (EoR). The evolution of the IGM opacity within the Ly $\alpha$  forest along quasar sightlines shows a steep rise around  $z \gtrsim 5.5$  as well as an increased scatter in the measurements (Fan et al. 2006; Becker et al. 2015; Bosman et al. 2018; Eilers et al. 2018), suggesting a qualitative change in the ionization state of the IGM provoked by a decrease in the ionizing ultraviolet background (UVB) radiation (Calverley et al. 2011; Wyithe & Bolton 2011; Dayal & Ferrera 2018; Davies et al. 2018b; Kulkarni et al. 2019).

The largest outliers in the IGM opacity measurements come from the detection of a very long Gunn–Peterson trough in the Ly $\alpha$  forest along the sightline of ULAS J0148+0600 extending down to  $z \sim 5.5$ . These outliers have been the subject of extensive modeling efforts, which provide evidence for either large coherent spatial fluctuations in the UVB (Davies & Furlanetto 2016; D’Aloisio et al. 2018), residual fluctuations in the temperature field (D’Aloisio et al. 2015, but see Keating et al. 2018), the imprint of rare but bright sources of ionizing

photons (Chardin et al. 2015, 2017), or “islands” of residual neutral gas as low as  $z \lesssim 5.5$  due to an extended, inhomogeneous reionization process (Kulkarni et al. 2019). Distinguishing these scenarios via the distribution of Ly $\alpha$  forest opacity alone is challenging (Davies et al. 2018a), although the recent discovery of a large-scale underdensity of Ly $\alpha$ -emitting galaxies around the ULAS J0148+0600 Gunn–Peterson trough seems to suggest that UVB fluctuations may be the culprit (Becker et al. 2018).

In this paper, we explore a different tracer co-spatial with the Ly $\alpha$  forest, namely the Ly $\beta$  forest. Whereas the overly sensitive Ly $\alpha$  transition saturates for neutral gas fractions of  $x_{\text{H I}} \gtrsim 10^{-4}$ , the  $\sim 5$  times lower oscillator strength of the Ly $\beta$  transition makes it more sensitive to gas with a higher neutral fraction and thus provides more stringent constraints on the IGM ionization state (e.g., Davies et al. 2018b), as well as on its thermal state (Oh & Furlanetto 2005; Trac et al. 2008; Furlanetto & Oh 2009).

This can be understood when having a closer look at the mean transmitted forest flux and the Gunn–Peterson optical depth  $\tau$ . Assuming a volume-weighted probability density function for IGM physical conditions (e.g., Faucher-Giguère et al. 2008a), we can write mean flux over some spatial interval as

$$\langle F \rangle(z) = \int_0^\infty \int_0^\infty \int_0^\infty d\Delta dT d\Gamma_{\text{H I}} P(\Delta, T, \Gamma_{\text{H I}}|z) \exp(-\tau_i), \quad (1)$$

where

$$\tau_i \propto n_{\text{H I}} \propto n_{\text{H}} x_{\text{H I}} \propto \frac{\Delta^2 T^{-0.7}}{\Gamma_{\text{H I}}}. \quad (2)$$

is the opacity in either the  $\text{Ly}\alpha$  or  $\text{Ly}\beta$  transition, and  $\Gamma_{\text{H I}}$  is the ionization rate of the UVB. Owing to the difference in their oscillator strengths, the two transitions take different distinct “moments” of the distribution  $P(\Delta, T, \Gamma_{\text{H I}}|z)$  encapsulating IGM physical conditions (see also Figure 6 of Furlanetto & Oh (2009)).

In accordance with the standard paradigm for the thermal state of the post-reionization photoionized IGM, we expect that the majority of the optically thin gas responsible for the absorption in the  $\text{Ly}\alpha$  and  $\text{Ly}\beta$  forests follows a tight relation between the gas density  $\rho$  and its temperature  $T$ , the “equation of state,” which arises from a balance between photoheating and the aggregate effect of recombination, inverse Compton cooling, and adiabatic cooling due to the expansion of the universe:

$$T = T_0 \left( \frac{\rho}{\rho_0} \right)^{\gamma-1}, \quad (3)$$

where  $T_0$  denotes the temperature at average density  $\rho_0$  (Hui & Gnedin 1997; McQuinn & Upton Sanderbeck 2016). A slope with  $\gamma < 1$  denotes an inverted temperature–density relation, implying that underdense voids are hotter than overdense regions in the IGM, while  $\gamma = 1$  represents an isothermal temperature–density relation. One can expect to find a fiducial value of  $\gamma \approx 1.5$ – $1.6$  for the IGM long after any reionization events (Hui & Gnedin 1997; McQuinn & Upton Sanderbeck 2016).

However, during and immediately after reionization events, a flat or inverted temperature–density relation is predicted by several studies using hydrodynamical simulations that model the reionization process self-consistently. Trac et al. (2008) showed that the gas near large overdensities ionizes and heats up earlier than the gas in underdense voids, and hence the IGM temperature is inversely proportional to the reionization redshift. Thus, an inverted equation of state naturally arises at the end of the reionization epoch, although with a large scatter. In their late reionization scenario, in which reionization completes at  $z \sim 6$ , an inverted or isothermal temperature–density relation of the low-density gas in the IGM persists until  $z \sim 4$ . These results have later been reproduced by Finlator et al. (2018), who model the EoR with an inhomogeneous UVB radiation field and find that an isothermal temperature–density relation endures well past the end of the reionization process.

Furlanetto & Oh (2009) explore the effects of an inhomogeneous reionization process on the temperature–density relation of the IGM with an analytic model, and also predict an inversion of the equation of state during the EoR. They find a degeneracy between a rapidly evolving UVB and temperature field, and conclude that a wider range of densities and different effective temperatures probed by the higher Lyman-series forests is necessary to set tighter constraints on the thermal state of the IGM.

While several authors have measured the evolution of  $\text{Ly}\alpha$  and  $\text{Ly}\beta$  opacity and their implications for the neutral gas fraction of the IGM (Lidz et al. 2002; Songaila 2004; Fan et al. 2006), the correspondence between  $\text{Ly}\alpha$  and  $\text{Ly}\beta$  opacities has not yet been studied in detail. Here, we address this matter and measure the IGM opacity in both the  $\text{Ly}\alpha$  and the  $\text{Ly}\beta$  forest toward the end of the reionization epoch between  $5.5 \leq z \leq 6.1$  along 19 quasar sightlines that have signal-to-noise ratio (S/N)  $\gtrsim 10$  per pixel and do not show any broad absorption line signatures. We present our data set and the

applied methods to measure the IGM opacity in Section 2, whereas our final measurements are shown in Section 3. In Section 4, we introduce various models of the physical conditions in the post-reionization IGM, which we obtain by post-processing of the `Nyx` cosmological hydrodynamical simulation, and conduct a comparison between our results and the predictions from these models. We discuss the implications of our results on the EoR in Section 5, before summarizing our main findings in Section 6. Throughout this paper, we assume a cosmology of  $h = 0.685$ ,  $\Omega_{\text{m}} = 0.3$  and  $\Omega_{\Lambda} = 0.7$ , which is consistent within the  $1\sigma$  error bars with Planck Collaboration et al. (2018).

## 2. Methods

### 2.1. The Quasar Sample

Our original data sample comprises 34 quasar spectra at  $5.77 \leq z_{\text{em}} \leq 6.54$  and has been publicly released (Eilers et al. 2018) via the `igmspec` database (Prochaska 2017) and the `zenodo` platform.<sup>5</sup> Previously, we have used this data set to analyze the sizes of quasar proximity zones (Eilers et al. 2017a), as well as the redshift evolution of the IGM opacity within the  $\text{Ly}\alpha$  forest (Eilers et al. 2018). For the study of the joint  $\text{Ly}\alpha$  and  $\text{Ly}\beta$  forest opacity that we present in this paper, we take a subset of 19 quasar spectra with  $\text{S/N} \geq 10$  per  $10 \text{ km s}^{-1}$  pixel. All spectra have been observed at optical wavelengths (4000–10000 Å) with the Echellette Spectrograph and Imager (ESI; Sheinis et al. 2002) at the Keck II Telescope between the years of 2001 and 2016. The data were collected from the Keck Observatory Archive<sup>6</sup> and complemented with our own observations. All observations used slit widths ranging from  $0''.75$  to  $1''.0$ , resulting in a resolution of  $R \approx 4000$ – $5400$ .

The details of all individual observations as well as detailed information about the data reduction process can be found in Eilers et al. (2017a, 2018). We make further improvements on our data reduction in order to avoid biases in our analysis of the opacities within the  $\text{Ly}\beta$  forest *relative* to the opacities within the  $\text{Ly}\alpha$  forest, which could arise due to potential flux calibration issues or in the process of coadding individual exposures. Hence, we correct all final extracted and coadded spectra with a power law, if necessary, to match the observed photometry in the  $i$ - and  $z$ -band (see Appendix A for details on this procedure). The properties of all quasars in our data sample are listed in Table 1 in Eilers et al. (2018).

### 2.2. Continuum Normalization

We normalize the quasar spectra by their continuum emission, which we estimate using a principal component analysis (PCA) reconstruction. The idea of the PCA is for each continuum spectrum to be represented by a mean spectrum plus a finite number of weighted principal component spectra (Suzuki et al. 2005; Suzuki 2006; Pâris et al. 2011). Because the quasar spectra in our data set experience substantial absorption blueward of the  $\text{Ly}\alpha$  emission line from intervening neutral hydrogen in IGM, we follow the procedure suggested by Pâris et al. (2011) and estimate the coefficients for the reconstructed continuum emission using only pixels redward of the  $\text{Ly}\alpha$  line, and then apply a projection matrix to obtain the

<sup>5</sup> <https://doi.org/10.5281/zenodo.1467821>

<sup>6</sup> <https://koa.ipac.caltech.edu/cgi-bin/KOA/nph-KOAlogin>

coefficients for the continuum spectrum covering the whole spectral range between  $1020 \text{ \AA} \leq \lambda_{\text{rest}} \leq 1600 \text{ \AA}$ . Because the PCA components do not cover bluer wavelengths, we extend the estimated continuum to bluer wavelengths by appending the composite quasar spectrum from Shull et al. (2012) continuously at  $\lambda_{\text{rest}} < 1020 \text{ \AA}$ ; for details, see Eilers et al. (2018).

### 2.3. The Effective Optical Depth

We estimate the opacity of the IGM by means of the effective optical depth, i.e.,

$$\tau_{\text{eff}} = -\ln\langle F \rangle, \quad (4)$$

where  $\langle F \rangle$  denotes the continuum normalized transmitted flux averaged over discrete spectral bins along the line of sight to each quasar. In this study, we choose spectral bins of 40 cMpc, instead of a bin size of 50 cMpc  $h^{-1}$  used in previous work (Becker et al. 2015; Bosman et al. 2018; Eilers et al. 2018). This smaller bin is chosen such that the Ly $\beta$  forest region is better sampled. Note that whenever the average flux  $\langle F \rangle$  is negative or detected with less than  $2\sigma$  significance, we adopt a lower limit on the optical depth at the  $2\sigma$  level, in accordance with previous work (Fan et al. 2006; Becker et al. 2015).

The Ly $\alpha$  forest lies between the Ly $\alpha$  and Ly $\beta$  emission lines at the rest-frame wavelengths  $\lambda_{\text{Ly}\alpha} = 1215.67 \text{ \AA}$  and  $\lambda_{\text{Ly}\beta} = 1025.72 \text{ \AA}$ , respectively, whereas the Ly $\beta$  forest covers the wavelength region between the Ly $\beta$  and the Ly $\gamma$  (at rest-frame wavelength  $\lambda_{\text{Ly}\gamma} = 972.54 \text{ \AA}$ ) emission lines. However, we do not conduct the IGM opacity measurements within the whole wavelength region, but the proximity zones around each quasar are excluded as in Eilers et al. (2018), i.e., we mask the region around each quasar that is heavily influenced by the quasar’s own radiation, resulting in enhanced transmitted flux. Additionally, we choose the rest-frame wavelengths 1030 and 975  $\text{\AA}$  as the respective minimum wavelengths for our measurements in the Ly $\alpha$  and Ly $\beta$  forest. Thus, for a typical quasar at  $z_{\text{em}} \sim 6$  with a proximity zone of  $R_p \approx 5 \text{ pMpc}$ , we measure the opacity of the Ly $\alpha$  and Ly $\beta$  forests between the observed wavelengths 7210–8389  $\text{\AA}$  and 6825–7078  $\text{\AA}$ , respectively.

Additionally, as described in detail in Eilers et al. (2018), we correct for small offsets in the zero level of each spectrum that might have been introduced due to improper sky subtraction, and mask the spectral regions around DLAs, in order to avoid any biases in the estimation of the IGM opacity.<sup>7</sup>

Note that we do not attempt to correct for any metal line contamination within the Ly $\alpha$  and Ly $\beta$  forests. Faucher-Giguère et al. (2008b) show in their Figure 8 that the relative metal correction to  $\tau_{\text{eff}}$  in the Ly $\alpha$  forest decreases with increasing redshift from 13% at  $z = 2$ –5% at  $z = 4$ . Assuming a monotonic increase in the enrichment of the IGM with time, we expect to have a negligible metal contamination at  $z \approx 6$ .

### 3. Measurements of the IGM Opacity

For a quasar at redshift  $z_{\text{em}}$ , we encounter foreground Ly $\alpha$  forest absorption from the IGM at lower redshift, i.e.,  $z_{\text{fg}}$ , within the observed wavelength range of the Ly $\beta$  forest, i.e.,

$$z_{\text{fg}} = \left( (1 + z_{\text{em}}) \frac{\lambda_{\text{Ly}\beta}}{\lambda_{\text{Ly}\alpha}} \right) - 1. \quad (5)$$

The redshift range of the foreground Ly $\alpha$  forest absorption within the Ly $\beta$  forest is  $z_{\text{fg}} \approx 4.61$ –4.82 for a quasar at  $z_{\text{em}} \approx 6$ .

In this paper, we calculate the effective optical depth by means of Equation (4) in the Ly $\alpha$  forest  $\tau_{\text{eff}}^{\text{Ly}\alpha}$  as well as the *observed* effective optical depth in the Ly $\beta$  forest  $\tau_{\text{eff}}^{\text{Ly}\beta, \text{obs}}$ , which includes the absorption from the foreground Ly $\alpha$  forest. Hence, we do not attempt to “correct” the Ly $\beta$  opacity measurements by subtracting the foreground Ly $\alpha$  absorption, but rather analyze the observed Ly $\beta$  opacity, which is the sum of the *pure* Ly $\beta$  optical depth and the Ly $\alpha$  forest opacity in the foreground IGM. We measure both effective optical depths within the Ly $\alpha$  and the Ly $\beta$  forest in discrete spectral bins around the same central redshift  $z_{\text{abs}}$ . Our chosen bin size of 40 cMpc allows us to obtain two estimates along each quasar sight line, in the absence of any masked spectral bins due to intervening DLAs.

The resulting measurements of the effective optical depths along the 19 quasar sight lines in our data sample are listed in Table 1. The redshift evolution of the observed effective optical depth in the Ly $\beta$  forest is presented in Figure 1. We also show the mean values,  $\langle \tau_{\text{eff}}^{\text{Ly}\beta, \text{obs}} \rangle$ , in bins of  $\Delta z = 0.2$ , which are listed in Table 2, as well as a compilation of all Ly $\beta$  measurements from the literature (Fan et al. 2006; Willott et al. 2007; Barnett et al. 2017; Tang et al. 2017). We find a sharp increase in the observed Ly $\beta$  optical depth for  $z \gtrsim 5.8$ , which is in agreement with previous results (Lidz et al. 2002; Songaila 2004; Fan et al. 2006).

The gray bands underlying the measurements in Figure 1 show the expected redshift evolution of the Ly $\beta$  opacity from the *Nyx* cosmological hydrodynamical simulation (see Section 4 for details), with a default value of  $\gamma = 1.5$  for the slope of the temperature–density relation (Hui & Gnedin 1997; Upton Sanderbeck et al. 2016). The light and medium gray bands show the expected  $1\sigma$  and  $2\sigma$  scatter, whereas the thin dark gray band presents any additional scatter expected from  $\sim 20\%$  uncertainties in the quasar continuum estimates, which only have a small effect (Becker et al. 2015; Eilers et al. 2017b). As noticed in multiple previous studies (e.g., Fan et al. 2006; Becker et al. 2015; Bosman et al. 2018; Eilers et al. 2018), the observed scatter is larger than expected from a homogeneous reionization model, in which density fluctuations alone account for the scatter in the opacities, which gave rise to models with spatial fluctuations in the UVB or the underlying temperature field, which we will introduce in Sections 4.1 and 4.2.

A few selected spectral bins along four different quasar sightlines, showing the transmitted flux in the Ly $\alpha$  forest and the respective co-spatial region in the Ly $\beta$  forest, are shown as examples in Figure 2. The spectral bins depicted here were chosen because they are particularly opaque in the Ly $\beta$  forest. All other remaining spectral bins in our data sample are shown in Figures 9 and 10 in Appendix B. The red data points in each panel show the *measured* mean flux in the respective spectral

<sup>7</sup> Note that the masking of bins containing a DLA removes all bins within the Ly $\beta$  forest along two quasar sightlines, i.e., SDSS J0100+2802 and SDSS J1148+5251.

**Table 1**  
Mean Flux Measurements in the Ly $\alpha$  and Ly $\beta$  Forest

Object	$z_{\text{em}}$	$z_{\text{start}}$	$z_{\text{abs}}$	$z_{\text{end}}$	$\langle F^{\text{Ly}\alpha} \rangle$	$\langle F^{\text{Ly}\beta, \text{obs}} \rangle$
SDSSJ0002+2550	5.82	5.699	5.656	5.613	$0.0728 \pm 0.0005$	$0.0563 \pm 0.0005$
SDSSJ0005-0006	5.844	5.613	5.570	5.528	$0.0245 \pm 0.0006$	$0.0752 \pm 0.0005$
		5.761	5.717	5.674	$0.0582 \pm 0.0022$	$0.1205 \pm 0.0066$
CFHQSJ0050+3445	6.253	5.674	5.631	5.588	$0.0484 \pm 0.0027$	$0.1580 \pm 0.0067$
		6.136	6.088	6.041	$0.0027 \pm 0.0025$	$-0.0018 \pm 0.0079$
ULASJ0148+0600	5.98	6.041	5.994	5.948	$0.0101 \pm 0.0031$	$0.0190 \pm 0.0046$
		5.842	5.797	5.753	$-0.0022 \pm 0.0032$	$-0.0032 \pm 0.0014$
PSOJ036+03	6.5412	5.753	5.709	5.666	$0.0028 \pm 0.0021$	$-0.0059 \pm 0.0014$
		6.421	6.370	6.320	$0.0010 \pm 0.0021$	$0.0104 \pm 0.0023$
PSOJ060+25	6.18	6.320	6.271	6.222	$-0.0034 \pm 0.0021$	$0.0183 \pm 0.0024$
		6.064	6.017	5.971	$0.0623 \pm 0.0039$	$0.0327 \pm 0.0028$
SDSSJ0836+0054	5.81	5.971	5.925	5.879	$0.0163 \pm 0.0081$	$0.0221 \pm 0.0023$
		5.695	5.652	5.609	$0.1323 \pm 0.0003$	$0.1765 \pm 0.0006$
SDSSJ0840+5624	5.8441	5.609	5.566	5.524	$0.0887 \pm 0.0005$	$0.1416 \pm 0.0005$
		5.692	5.648	5.606	$0.0124 \pm 0.0013$	$0.0379 \pm 0.0014$
SDSSJ1030+0524	6.309	6.061	6.014	5.968	$0.0018 \pm 0.0022$	$-0.0156 \pm 0.0018$
		6.156	6.108	6.061	$0.0097 \pm 0.0020$	$-0.0136 \pm 0.0050$
SDSSJ1137+3549	6.03	5.785	5.741	5.697	$0.0068 \pm 0.0031$	$0.1342 \pm 0.0022$
		5.874	5.829	5.785	$0.0126 \pm 0.0040$	$0.0378 \pm 0.0021$
SDSSJ1306+0356	6.016	5.797	5.752	5.709	$0.0486 \pm 0.0015$	$0.0418 \pm 0.0010$
		5.887	5.842	5.797	$0.1467 \pm 0.0022$	$0.0581 \pm 0.0010$
ULASJ1319+0950	6.133	5.932	5.887	5.841	$0.0265 \pm 0.0089$	$0.0207 \pm 0.0024$
		6.025	5.978	5.932	$-0.0021 \pm 0.0064$	$0.0082 \pm 0.0026$
SDSSJ1411+1217	5.904	5.792	5.748	5.704	$0.0131 \pm 0.0012$	$0.0087 \pm 0.0008$
		5.704	5.661	5.618	$0.0362 \pm 0.0011$	$0.0465 \pm 0.0008$
SDSSJ1602+4228	6.09	5.929	5.883	5.838	$0.0136 \pm 0.0040$	$0.0191 \pm 0.0013$
		5.838	5.794	5.749	$0.0604 \pm 0.0043$	$0.0784 \pm 0.0014$
SDSSJ1630+4012	6.065	5.852	5.807	5.763	$0.0366 \pm 0.0071$	$0.0771 \pm 0.0028$
		5.946	5.900	5.855	$0.0519 \pm 0.0055$	$0.0743 \pm 0.0047$
SDSSJ2054-0005	6.0391	5.855	5.810	5.765	$0.0085 \pm 0.0059$	$0.0414 \pm 0.0045$
		6.012	5.965	5.919	$-0.0073 \pm 0.0040$	$-0.0068 \pm 0.0036$
SDSSJ2315-0023	6.117	5.919	5.874	5.829	$-0.0135 \pm 0.0073$	$-0.0038 \pm 0.0034$

**Note.** The columns show the name of the object and its emission redshift  $z_{\text{em}}$ , the start of the redshift bin  $z_{\text{start}}$ , the mean redshift of each bin  $z_{\text{abs}}$ , and the end of each bin  $z_{\text{end}}$ , as well as the measured mean flux of the continuum normalized spectra in the Ly $\alpha$  and Ly $\beta$  forest.

bin, whereas the blue dotted lines and shaded regions in the bottom panels represent the *expected* mean and 68th percentile of flux in the Ly $\beta$  forest given the corresponding  $\tau_{\text{eff}}^{\text{Ly}\alpha}$  measurement shown in the top panels, assuming a model of the post-reionization IGM with a fluctuating UVB (see Section 4.1). The model predicts generally higher mean fluxes than measured in these selected spectral bins, which is an important issue that we will discuss in detail in Section 5.

#### 4. Models of the Post-reionization IGM

Several previous studies have shown that the scatter in the Ly $\alpha$  optical depth measurements of the IGM cannot be explained by fluctuations in the underlying density field alone; rather, it requires a spatially inhomogeneous reionization scenario with additional large-scale fluctuations in the UVB or the temperature field to reproduce the observations (Becker et al. 2015; Bosman et al. 2018; D’Aloisio et al. 2019; Davies et al. 2018b; Eilers et al. 2018). In this work, we compare these different physical models of the post-reionization IGM to the co-spatial opacity measurements in the Ly $\alpha$ , as well as the Ly $\beta$  forest.

All reionization models that we consider make use of the  $\text{Nyx}$  cosmological hydrodynamical simulation with  $100 \text{ cMpc } h^{-1}$  on a side and  $4096^3$  dark matter particles and gas elements on a uniform Eulerian grid, which was designed for precision studies of

the Ly $\alpha$  forest (Almgren et al. 2013; Lukić et al. 2015). We extract skewers of density, temperature, and velocity along the directions of the grid axes from simulation outputs at  $3.0 \leq z \leq 6.5$  in steps of  $\Delta z = 0.5$ . The outputs at lower redshifts are used to model the contamination of the Ly $\beta$  forest opacity by foreground Ly $\alpha$  absorption, which we will describe in Section 4.4. For redshifts in between the simulation outputs, we take the closest output and rescale the density field by  $(1+z)^3$  accordingly. The simulation adopts the uniform UVB model from Haardt & Madau (2012), resulting in an IGM model which (uniformly) reionized at early times, i.e.,  $z_{\text{reion}} > 10$  (Lukić et al. 2015; Oñorbe et al. 2017a). In Appendix C, we perform a set of convergence tests for the optical depth in the Ly $\beta$  forest at high redshift. The convergence of the Ly $\alpha$  forest has been tested previously in Oñorbe et al. (2017b).

First, we model the post-reionization IGM with a spatially inhomogeneous UVB (Section 4.1), and second, we assume a spatially fluctuating temperature field in the IGM (Section 4.2). Neither of these models reproduces our observations very well. We also consider a model with a uniform UVB, but vary the slope of the temperature–density relation of the IGM (Section 4.3). For each model, we will then calculate the optical depths along skewers through the simulation box (Section 4.4) and forward model the spectral noise of our data set onto the skewers (Section 4.5).



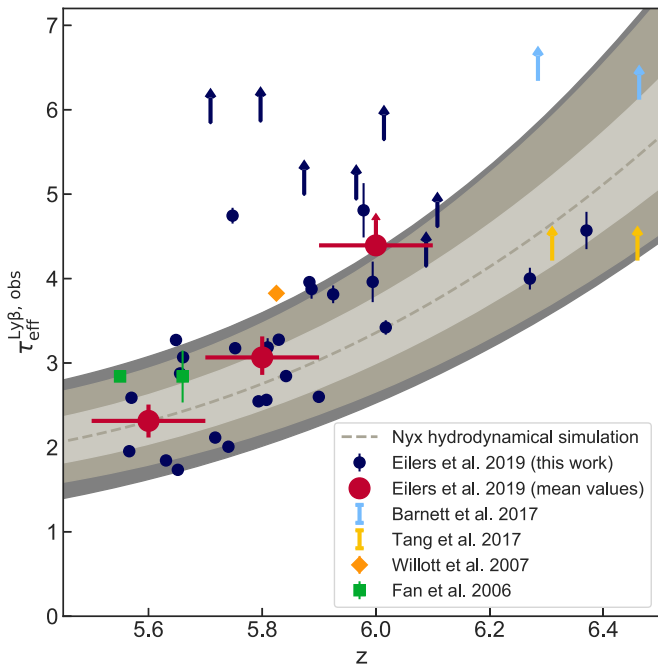


**Figure 1.** Evolution of the observed  $\text{Ly}\beta$  optical depth with redshift. The dark blue data points show our measurements of  $\tau_{\text{eff}}^{\text{Ly}\beta, \text{obs}}$ , whereas the large red data points represent the opacity measurements averaged over bins of  $\Delta z = 0.2$ , with uncertainties determined via bootstrapping. Otherwise, colored data points show all  $\text{Ly}\beta$  optical depth measurements found in the literature along quasar sightlines that are not part of our data sample. Note, however, that the chosen spectral bin size here varies between different analyses. The gray underlying region shows the predicted redshift evolution from the Nyx hydrodynamical simulation assuming a uniform UVB. We have simulation outputs in steps of  $\Delta z = 0.5$ , and use a cubic spline function to interpolate the shaded regions between the redshift outputs. The light and medium gray shaded regions indicate the 68th and 95th percentiles of the scatter expected from density fluctuations in the simulations, whereas the dark gray regions show any additional scatter due to  $\sim 20\%$  continuum uncertainties.

**Table 2**

Measurements of the Average Flux and Optical Depth within the  $\text{Ly}\beta$  Forest

$z_{\text{abs}}$	$\langle F^{\text{Ly}\beta, \text{obs}} \rangle$	$\sigma_{(F^{\text{Ly}\beta, \text{obs}})}$	$\langle \tau_{\text{eff}}^{\text{Ly}\beta, \text{obs}} \rangle$	$\sigma_{(\tau_{\text{eff}}^{\text{Ly}\beta, \text{obs}})}$
5.6	0.0989	0.0193	2.3140	0.1952
5.8	0.0466	0.0106	3.0658	0.2279
6.0	0.0082	0.0062	$>4.3935$	...

**Note.** The rows show the mean redshift  $z_{\text{abs}}$  of the redshift bins of size  $\Delta z = 0.2$ , the averaged flux  $\langle F^{\text{Ly}\beta, \text{obs}} \rangle$  and its uncertainty  $\sigma_{(F^{\text{Ly}\beta, \text{obs}})}$  determined via bootstrapping, and the mean optical depth  $\langle \tau_{\text{eff}}^{\text{Ly}\beta, \text{obs}} \rangle$  in that redshift bin and its error  $\sigma_{(\tau_{\text{eff}}^{\text{Ly}\beta, \text{obs}})}$ , also determined via bootstrapping.

#### 4.1. Fluctuating UVB

We first compare our measurements to predictions of the  $\text{Ly}\beta$  forest opacity from a published reionization model with a spatially inhomogeneous UVB by Davies et al. (2018b). The model consists of UVB fluctuations from an independent seminumerical simulation following Davies & Furlanetto (2016), which we summarize briefly here. First, using the 21cmFAST code, we generated a set of cosmological initial conditions in a  $(400 \text{ cMpc})^3$  volume. From these initial conditions, we derived the locations of dark matter halos following the excursion set method of Mesinger & Furlanetto (2007), and shifted their positions to  $z = 6$  with the Zel’dovich approximation (Zel’dovich 1970). The UV luminosities of the

halos were then computed via abundance matching (e.g., Vale & Ostriker 2004) to the Bouwens et al. (2015) UV luminosity function. Finally, the ionizing radiation field was computed assuming a halo mass-independent conversion from UV luminosity to ionizing luminosity, and a spatially varying mean free path of ionizing photons (Davies & Furlanetto 2016). We then impose the fluctuating UVB onto the Nyx skewers and recompute the ionization state of the gas assuming ionization equilibrium.

Because the UVB fluctuations were computed in an independent cosmological volume from the hydrodynamical simulation, this approach modestly overestimates the effect of UVB fluctuations on the IGM opacity because the anticorrelation between the UVB and the large-scale density field (Davies & Furlanetto 2016; Davies et al. 2018a) is lost. While small-scale correlations between the UVB and the density field may alter the relationship between  $\text{Ly}\alpha$  and  $\text{Ly}\beta$  forest opacity (Oh & Furlanetto 2005), the UVB fluctuations in the Davies et al. (2018a) model manifest on scales comparable to the size of our 40 cMpc bins, so we do not expect a substantial effect.

#### 4.2. Fluctuating Temperature Field of the IGM

In order to model temperature fluctuations, we use a new hybrid method introduced in Oñorbe et al. (2019) that uses a small set of phenomenological input parameters, and combines a seminumerical reionization model (21cmFAST; Mesinger et al. 2011) to solve for the topology of reionization, as well as an approximate model of how reionization heats the IGM, with the cosmological hydrodynamical code Nyx. Instead of applying a uniform UVB to the whole simulation box, which was the procedure in the original Nyx simulations, the UVB is now applied to denser regions in the simulations at earlier reionization redshifts  $z_{\text{reion}}$ , whereas the underdense voids will be reionized at later times. At the same time, the gas temperature is heated up. The topology of the different reionization times  $z_{\text{reion}}$  are extracted from the seminumerical model.

This guarantees that the temperature evolution of the inhomogeneous reionization process and the small-scale structure of the diffuse gas of the IGM is resolved and captured self-consistently. In this work, we used the IR-A reionization model presented in Oñorbe et al. (2019), which is an extended reionization model consistent with the observations of the cosmic microwave background (CMB) by Planck Collaboration et al. (2018) with a median reionization redshift of  $z_{\text{reion}} = 7.75$ , a duration of the reionization process of  $\Delta z_{\text{reion}} = 4.82$ , and a heat injection due to reionization of  $\Delta T = 20,000 \text{ K}$ . We apply this model to a Nyx simulation with  $L = 40 \text{ Mpc } h^{-1}$  box side and  $2048^3$  resolution elements. The full thermal evolution of this model at the redshifts of interest for this work can be seen in Figures 5 and 6 in Oñorbe et al. (2019).

#### 4.3. Varying the Slope of the Temperature–Density Relation in a Uniform IGM

We will see in Section 5 that neither of the two models described above provides a good fit to our opacity measurements in both the  $\text{Ly}\alpha$  and the  $\text{Ly}\beta$  forests. Because the ratio of these opacities is sensitive to the temperature–density relation of the IGM, we will also compare our measurements to models

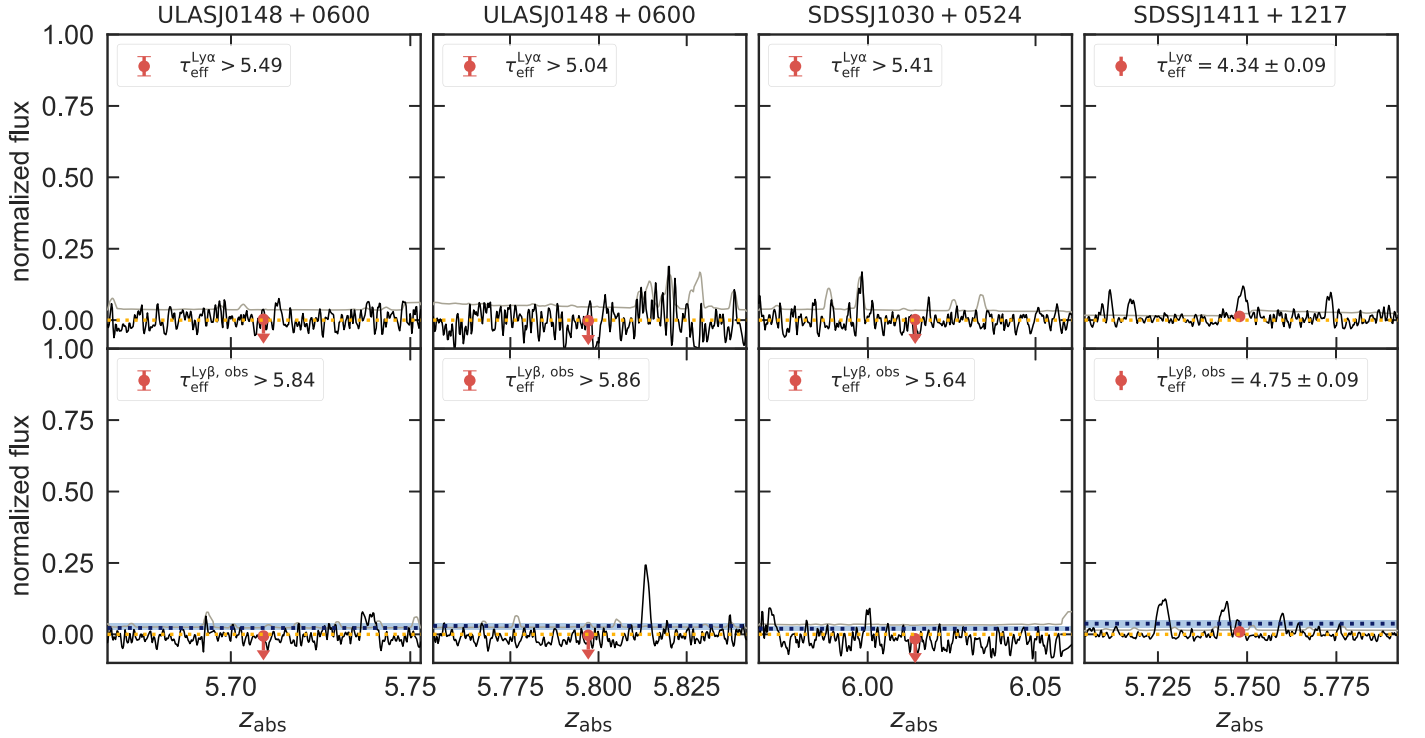


**Figure 2.** Selected spectral bins along four different quasar sightlines showing the transmitted flux (black) and the noise vector (gray) in the  $\text{Ly}\alpha$  forest (top panels) and the  $\text{Ly}\beta$  forest (lower panels) in a spectral bin centered around the same absorption redshift  $z_{\text{abs}}$ . The red data points indicate the measured mean fluxes  $\langle F \rangle$  in the respective bins and the corresponding optical depths are indicated in the legend. Note that the error bars on the mean fluxes are smaller than the symbols. The yellow dotted lines indicate the zero level of the flux. The blue dotted line and shaded bands in the lower panels show the expected mean flux and 68th percentile in the  $\text{Ly}\beta$  forest from a reionization model with a fluctuating UVB.

with a homogeneous IGM but different slopes  $\gamma - 1$  of the temperature–density relation (see Equation (3)).

To this end, we simply ignore the temperatures of the extracted  $N_{\text{yx}}$  skewers and calculate new temperatures in post-processing for the gas densities along each skewer by means of Equation (3), assuming  $T_0 = 10,000$  K. We then take the velocity skewers and map again the modified real space into redshift space to calculate mean fluxes and opacities.

#### 4.4. Calculating the Optical Depth from Simulated Skewers

We will compare our observations to the reionization models in three redshift bins with  $\Delta z = 0.2$  at the central redshifts of  $z = 5.6$ ,  $z = 5.8$ , and  $z = 6.0$ . At each redshift, we extract  $N_{\text{skew}} = 2000$  skewers from the simulation box of the same size as our measurements, i.e., 40 cMpc. It is well known that the  $\text{Ly}\alpha$  opacity depends on the unknown amplitude of the UVB  $\Gamma_{\text{HI}}$ , so we rescale the optical depth in the  $\text{Ly}\alpha$  forest to match the observations and determine this unknown parameter. For each skewer, we compute the mean flux, or equivalently, the effective optical depth according to

$$\begin{aligned} \langle F^{\text{Ly}\alpha} \rangle &= \langle \exp[-\tau_i^{\text{Ly}\alpha}] \rangle \\ &= \langle \exp[-A_0 \times \tau_i^{\text{Ly}\alpha, \text{unscaled}}] \rangle, \end{aligned} \quad (6)$$

where the angle brackets denote the average in the 40 cMpc bins. In the last equality, we introduce the scaling factor  $A_0$ , which provides the lever arm for tuning the photoionization rate of the UVB  $\Gamma_{\text{HI}}$  to match the observations.

Studies of the  $\text{Ly}\alpha$  forest at lower redshift, i.e.,  $2 < z < 5$ , typically tune  $A_0$  to match the mean flux. Because this study

focuses on comparing the distribution of mean fluxes (effective optical depths) in 40 cMpc bins, we instead determine the value of  $A_0$  by requiring the 25th percentile of the cumulative distribution of the mean flux to match the data. Specifically, for the data in any redshift bin, we can solve the equation  $P(>\langle F^{\text{Ly}\alpha} \rangle) = 0.25$  for  $\langle F^{\text{Ly}\alpha} \rangle$ . Our procedure for setting the unknown  $\Gamma_{\text{HI}}$  for any given model is then to vary  $A_0$  until the model matches the  $\langle F^{\text{Ly}\alpha} \rangle$  determined from the data for that redshift bin. From the cumulative distribution of values in Table 3 in Appendix B, we measure  $\langle F^{\text{Ly}\alpha} \rangle_{25\text{th}}(z = 5.6) \approx 0.0713$ ,  $\langle F^{\text{Ly}\alpha} \rangle_{25\text{th}}(z = 5.8) \approx 0.0363$ , and  $\langle F^{\text{Ly}\alpha} \rangle_{25\text{th}}(z = 6.0) \approx 0.0144$ . Note that the choice of the 25th percentile is somewhat arbitrary, and we could have also chosen to match the observed mean or median flux, which would not change any of the conclusions of this work.

We then obtain the *pure*  $\text{Ly}\beta$  optical depth  $\tau_i^{\text{Ly}\beta}$  at each pixel from  $\tau_i^{\text{Ly}\alpha}$  by scaling according to the oscillator strengths of their transitions and the respective wavelengths, i.e.,

$$\tau_i^{\text{Ly}\beta} = \frac{f_{\text{Ly}\beta}}{f_{\text{Ly}\alpha}} \frac{\lambda_{\text{Ly}\beta}}{\lambda_{\text{Ly}\alpha}} \tau_i^{\text{Ly}\alpha} \quad (7)$$

with  $f_{\text{Ly}\alpha} = 0.41641$  and  $f_{\text{Ly}\beta} = 0.079142$  (Table 4 in Wiese & Fuhr (2009)). This scaling is correct, provided that there are no damping wing effects due to the presence of very dense or highly neutral gas. Given that our analysis is focused on the low-density IGM at  $z \gtrsim 5.5$  probed by the  $\text{Ly}\alpha$  and  $\text{Ly}\beta$  forests at typical locations of the universe, this is a good approximation.

However, the *observed*  $\text{Ly}\beta$  effective optical depth  $\tau_{\text{eff}}^{\text{Ly}\beta, \text{obs}}$  will be higher than the pure  $\text{Ly}\beta$  optical depth, due to the

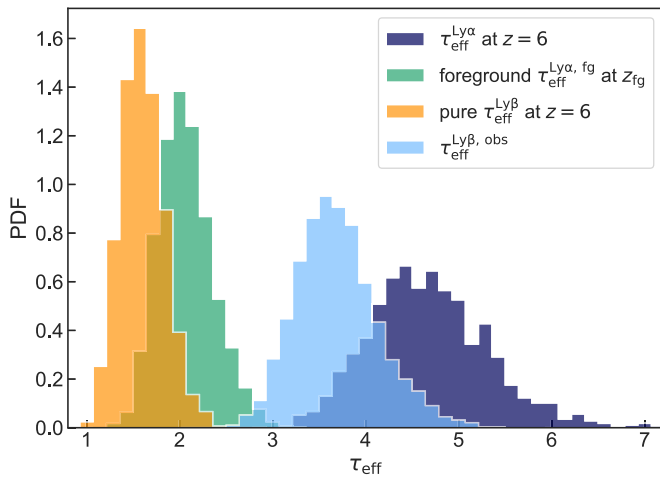


**Figure 3.** Distribution of  $\tau_{\text{eff}}$  values from 2000 skewers of the noise-free uniform reionization model with  $\gamma = 1.5$  at  $z = 6$ . The histograms show the distribution of  $\tau_{\text{eff}}^{\text{Ly}\alpha}$  at  $z = 6$  (dark blue), the distribution of  $\tau_{\text{eff}}^{\text{Ly}\alpha, \text{fg}}$  at the foreground redshift (green), the pure  $\tau_{\text{eff}}^{\text{Ly}\beta}$  values (yellow), and the distribution of observed  $\tau_{\text{eff}}^{\text{Ly}\beta, \text{obs}}$  values after accounting for the distribution of foreground Ly $\alpha$  opacities (light blue).

additional absorption from the Ly $\alpha$  forest at the foreground redshift. Thus, we create additional skewers along *different* lines of sight with Ly $\alpha$  forest absorption at the foreground redshift  $z_{\text{fg}}$ , i.e.,  $\tau_i^{\text{Ly}\alpha, \text{fg}}$ , using lower-redshift outputs from the N $\gamma$ x simulation. These lower-redshift skewers are also rescaled, but to match the mean flux in order to be consistent with published measurements. We use the fitting formula presented in Oñorbe et al. (2017a) to the mean flux measurements by Faucher-Giguère et al. (2008b), i.e.,  $\langle F^{\text{Ly}\alpha} \rangle(z_{\text{fg}} = 4.57) \approx 0.2371$ ,  $\langle F^{\text{Ly}\alpha} \rangle(z_{\text{fg}} = 4.74) \approx 0.1945$ , and  $\langle F^{\text{Ly}\alpha} \rangle(z_{\text{fg}} = 4.91) \approx 0.1560$  for the redshift bins at  $z = 5.6$ ,  $z = 5.8$ , and  $z = 6.0$ , respectively.

For each skewer of the high-redshift Ly $\beta$  forest, we now draw a *random* Ly $\alpha$  forest segment from a simulation output at the corresponding foreground redshift. In this way, we ensure that we account for the full distribution of foreground Ly $\alpha$  opacities, and do not underestimate the scatter between different foreground sightlines. At each pixel, we then sum the pure Ly $\beta$  forest optical depth with the foreground Ly $\alpha$  optical depth to obtain the flux one would observe in the Ly $\beta$  forest, i.e.,

$$F_i^{\text{Ly}\beta, \text{obs}} = \exp[-(\tau_i^{\text{Ly}\beta} + \tau_i^{\text{Ly}\alpha, \text{fg}})]. \quad (8)$$

We calculate the observed effective Ly $\beta$  optical depth by averaging the flux of all pixels in the spectral bin, i.e.,  $\tau_{\text{eff}}^{\text{Ly}\beta, \text{obs}} = -\ln \langle F_i^{\text{Ly}\beta, \text{obs}} \rangle$ .

Figure 3 shows the various distributions of effective optical depths in an example case for the uniform reionization model with  $\gamma = 1.5$  at  $z = 6$ , but all other models look qualitatively similar. The dark blue histogram shows the distribution of  $\tau_{\text{eff}}^{\text{Ly}\alpha}$  at  $z = 6$ , whereas the green histogram depicts the distribution of  $\tau_{\text{eff}}^{\text{Ly}\alpha, \text{fg}}$  along different skewers at the foreground redshift  $z_{\text{fg}} \approx 4.9$ . The yellow histogram shows the pure  $\tau_{\text{eff}}^{\text{Ly}\beta}$  values obtained from rescaling according to Equation (6), while the light blue histogram represents the distribution of observed  $\tau_{\text{eff}}^{\text{Ly}\beta, \text{obs}}$  values after accounting for the distribution of foreground Ly $\alpha$  opacities.

#### 4.5. Forward Modeling of Spectral Noise

The spectral noise in the data influences the opacity measurements. This is because whenever the average flux is detected with less than  $2\sigma$  significance, we adopt a lower limit on the effective optical depth measurement (see Section 2.3). To mimic the effects of the noisy data, for each mean flux value  $\langle F_{\text{sim}} \rangle$  from the simulated skewers, we randomly draw an uncertainty  $\sigma_{\langle F_{\text{data}} \rangle}$  from the measurements from our data set. Note that the noise level formally depends on the signal, but in the limit where the objects are fainter than the sky, which is almost always the case for the highly absorbed forests in high-redshift quasars, the noise is dominated by the sky background and read noise rather than the object photon noise, so this is a good approximation.

For this mock data with forward-modeled noise, we then apply the same criterion as for the real data and adopt a measurement only if  $\langle F_{\text{sim}} \rangle \geq 2\sigma_{\langle F_{\text{data}} \rangle}$ , or a lower limit at  $2\sigma_{\langle F_{\text{data}} \rangle}$  otherwise. This reduces the sensitivity to very high opacities in the simulated skewers, which we do not have in noisy data.

### 5. Discussion

#### 5.1. Comparison to Inhomogeneous Reionization Models

We compare our co-spatial measurements of  $\tau_{\text{eff}}^{\text{Ly}\alpha}$  and  $\tau_{\text{eff}}^{\text{Ly}\beta, \text{obs}}$  to predictions from the various models of the post-reionization IGM in three different redshift bins centered around  $z = 5.6$ ,  $5.8$ , and  $6.0$  in Figure 4. The contours in the middle and bottom panels show the predicted parameter space from models with spatial fluctuations in the UVB and the temperature field, respectively. Note that we did not yet forward model the spectral noise in the data to the simulations here, because we are overlaying the data with error bars and indicating limits. Thus, for this qualitative comparison, forward modeling the noise would amount to effectively double counting the noise.

While our measurements fall within the predicted parameter space in the lowest-redshift bin, it is evident that the observed  $\tau_{\text{eff}}$  measurements in the two higher-redshift bins are not well confined to the predicted parameter space. The measured  $\tau_{\text{eff}}^{\text{Ly}\beta, \text{obs}}$  values show a larger scatter than expected by the models at  $z \sim 5.8$ , as well as an offset in the mean at  $z \sim 6$ .

Another way of illustrating this comparison is by means of the cumulative distribution function (CDF). In Figures 5 and 6, we present the CDFs of our opacity measurements as the red curves, as well as the predicted distributions from the post-reionization models including a fluctuating UVB and a fluctuating temperature field, respectively, as dotted black curves. Note that, whereas the measurements presented in Figure 4 are restricted to the spectral regions where we have co-spatial measurements of  $\tau_{\text{eff}}^{\text{Ly}\alpha}$  and  $\tau_{\text{eff}}^{\text{Ly}\beta, \text{obs}}$ , the cumulative histograms for  $\tau_{\text{eff}}^{\text{Ly}\alpha}$  in Figures 5 and 6 show *all* measurements from the full Ly $\alpha$  forests along all quasar sightlines in our data set.<sup>8</sup>

Both CDFs show clearly that, when fine-tuning the reionization models to match the observed transmission in the Ly $\alpha$  forest, the effective optical depth in the Ly $\beta$  forest is underestimated in the highest-redshift bin at  $z \sim 6$ . Additionally, as noted before, we find a large increase in the scatter of

<sup>8</sup> Whereas in Eilers et al. (2018) we used  $50 \text{ cMpc } h^{-1}$  bins, we recomputed the Ly $\alpha$  optical depths in  $40 \text{ cMpc}$  for the comparison here. These results are presented in Table 3 in Appendix B.

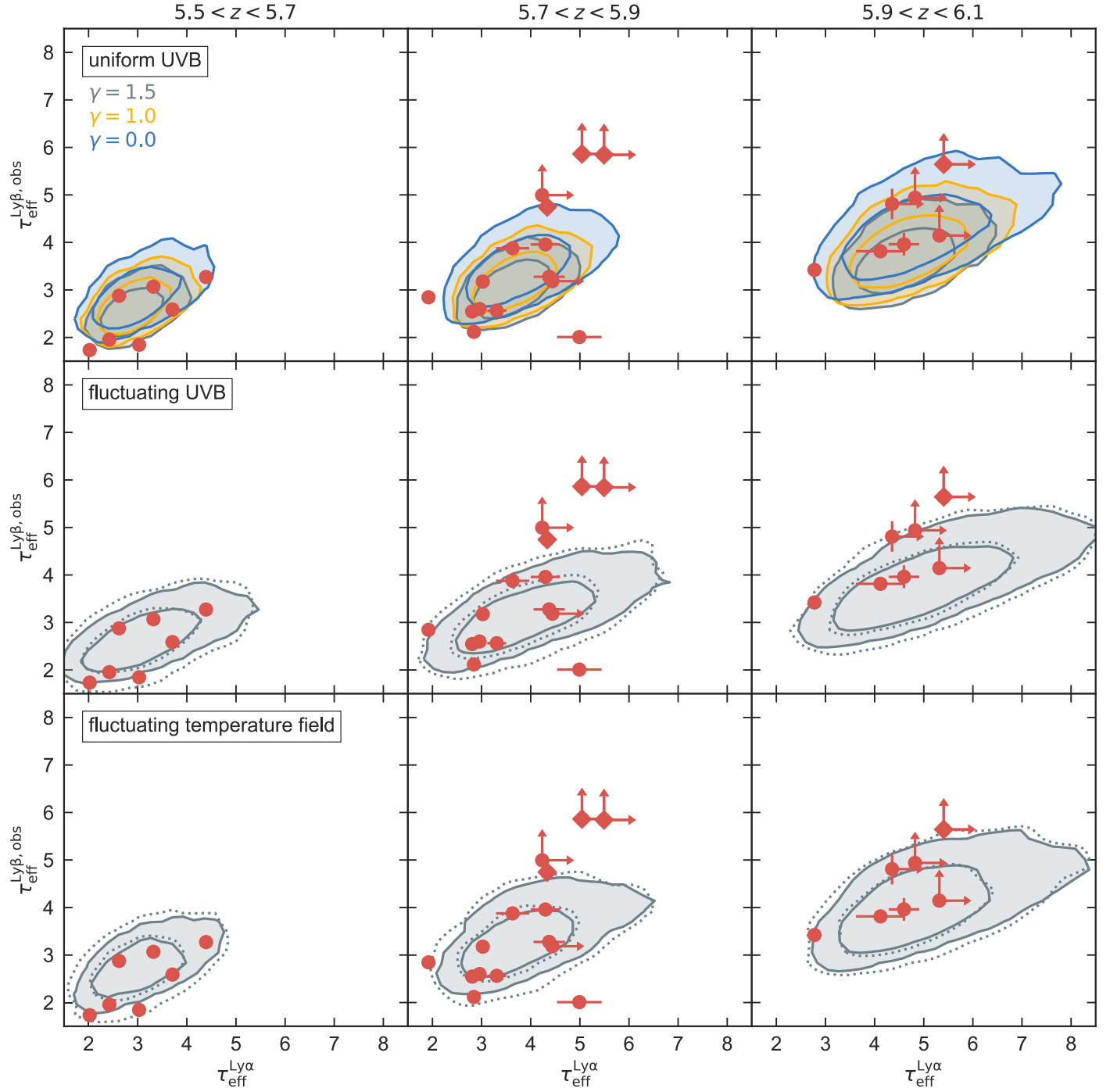


**Figure 4.** Comparison of our  $\text{Ly}\alpha$  and  $\text{Ly}\beta$  opacity measurements shown as the red data points in different redshift bins, i.e.,  $5.5 < z < 5.7$  (left),  $5.7 < z < 5.9$  (middle), and  $5.9 < z < 6.1$  (right), to predictions from the Nyx hydrodynamical simulation post-processed in several different ways. The contours in the top panels show the prediction from simulations with uniform UVB and different slopes of the temperature–density relation of the IGM, whereas the middle and bottom panels show predictions from models with a fluctuating UVB or a fluctuating temperature field, respectively. Inner and outer contours show the 68th and 95th percentile of the distribution. The dotted contours show the respective distributions including  $\sim 20\%$  continuum uncertainties (which we omitted in the top panels for better readability). The data points marked as diamonds correspond to the spectral bins shown in Figure 2.

the measurements, most notably at  $z \sim 5.8$ , compared to the predictions from the models.

Note that, in the two highest-redshift bins in Figure 5, the difference between the observed mean  $\text{Ly}\beta$  forest optical depth and the reionization model with a fluctuating UVB is  $\Delta\tau_{\text{eff}}^{\text{Ly}\beta} \gtrsim 1$ , which corresponds to a factor of  $\gtrsim 2.5$  in the mean flux. Hence, systematic uncertainties in the data that might arise from poor quasar continuum estimates or issues in

the data reduction process (see also Appendix A), would have to change the observed averaged flux by  $\gtrsim 250\%$  to account for this offset. This seems highly unlikely, as there is no obvious reason why such errors, if they were present, would be so asymmetric as to cause the flux in the  $\text{Ly}\beta$  region to be systematically lower by this large factor. Furthermore, if such systematics were present, they would presumably also impact the  $\text{Ly}\alpha$  measurements. However, a comparison of independent



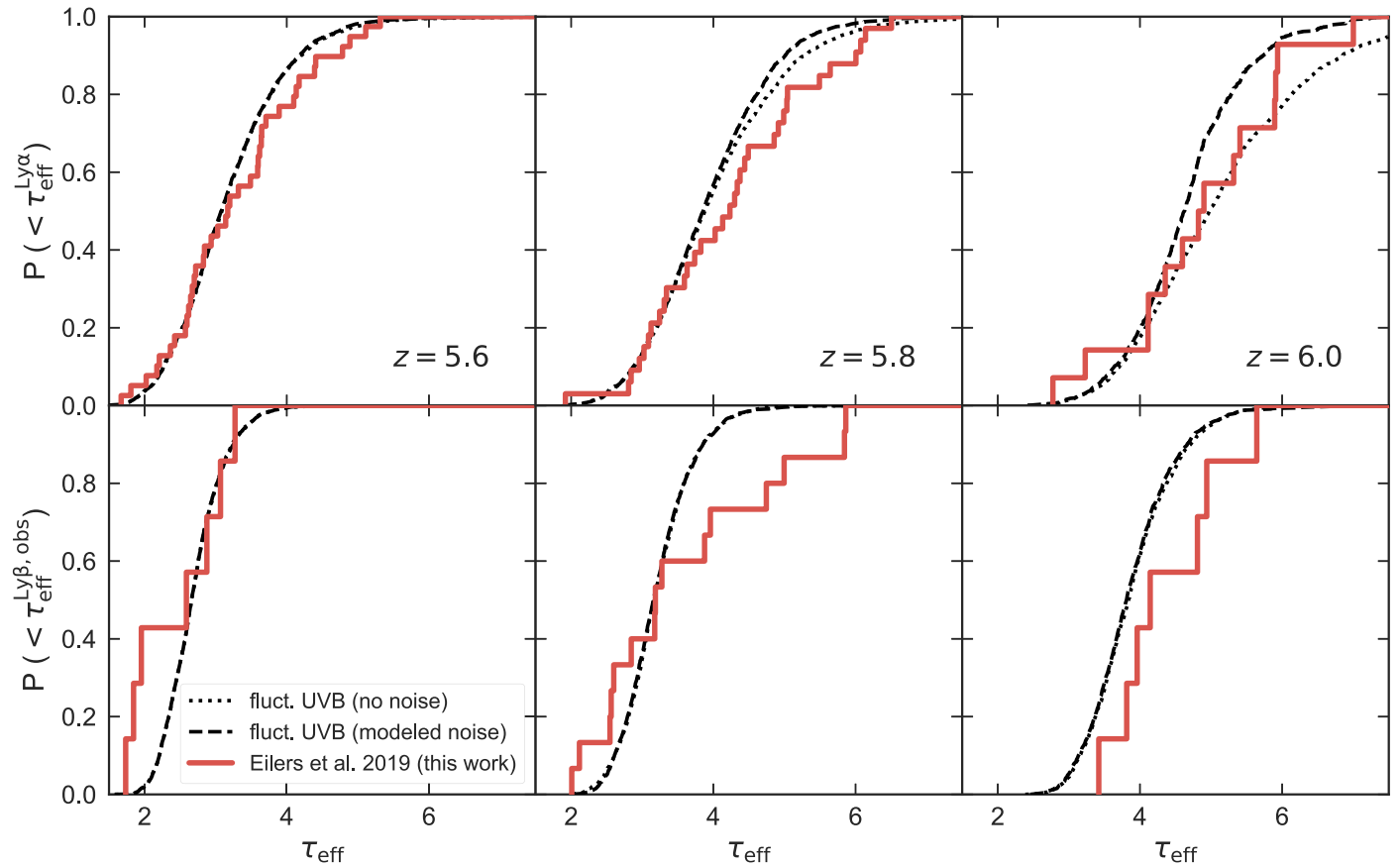


**Figure 5.** CDFs of  $\tau_{\text{eff}}^{\text{Ly}\alpha}$  (top panels) and  $\tau_{\text{eff}}^{\text{Ly}\beta, \text{obs}}$  (lower panels) in the same redshift bins as in Figure 4. Our measurements are shown in red, and the noise-free predictions from the reionization model with a fluctuating UVB is shown as the black dotted line. The black dashed curves show the same model, now including forward-modeled spectral noise. The models are scaled to match the 25th percentile of the observed  $\tau_{\text{eff}}^{\text{Ly}\alpha}$  distribution. Note that the top panels do not only contain the measurements of  $\tau_{\text{eff}}^{\text{Ly}\alpha}$  that have a corresponding  $\tau_{\text{eff}}^{\text{Ly}\beta, \text{obs}}$  measurement at the same redshift, but rather all measurements within the Ly $\alpha$  forest along all 19 quasar sight lines.

measurements of the distribution of  $\tau_{\text{eff}}^{\text{Ly}\alpha}$  between Bosman et al. (2018) and Eilers et al. (2018) (see Figure 7 in Eilers et al. (2018)) shows no evidence for systematic offsets of  $\Delta\tau_{\text{eff}}^{\text{Ly}\beta} \gtrsim 1$ . Note that the difference in Figure 6 between the mean Ly $\beta$  optical depth of the fluctuating temperature model predictions and the measurements is smaller, but still significant.

### 5.2. Evidence for an Inverted Temperature–Density Relation of the IGM

We know that the ratio of Ly $\alpha$  and Ly $\beta$  optical depths is sensitive to the ionization as well as the thermal state of the IGM (Oh & Furlanetto 2005; Trac et al. 2008; Furlanetto & Oh 2009). Thus, by varying the slope of the temperature–density relation of the intergalactic gas and adjusting it to be more isothermal (or inverted), we expect an increase in the predicted  $\tau_{\text{eff}}^{\text{Ly}\beta, \text{obs}}$ .

To this end, we also compare our observations to reionization models with a uniform IGM but different slopes of their temperature–density relations, i.e., the fiducial value of  $\gamma = 1.5$ , an isothermal temperature–density relation with  $\gamma = 1.0$ , and a highly inverted slope with  $\gamma = 0.0$ . This is shown in the top panels of Figure 4, as well as in Figure 7.

The comparison shows that the model with a highly inverted temperature–density relation, i.e.,  $\gamma = 0.0$ , predicts a higher

Ly $\beta$  opacity and seems to match the observations in the Ly $\beta$  forest in the highest-redshift bin better than the previously discussed inhomogeneous reionization models, although it is still not fully capturing the whole parameter space of the observations. Additionally, none of the uniform reionization models show enough spatial fluctuations to predict the scatter in the Ly $\alpha$  opacity.

How likely is it that the IGM follows an inverted temperature–density relation at  $z \sim 6$ ? It has been argued that reionization events dramatically alter the thermal structure of the IGM, increasing the IGM temperature by at least an order of magnitude up to  $T = 25,000\text{--}30,000$  K (Furlanetto & Oh 2009; D’Aloisio et al. 2019). Several hydrodynamical simulations that self-consistently model the reionization process have shown that a flat or inverted temperature–density relation arises naturally during reionization events, due to the different number densities of ionizing sources in over- and underdense regions (e.g., Trac et al. 2008; Finlator et al. 2018). The gas in dense regions ionizes first, due to the higher number of ionizing sources, and thus has more time to cool down, whereas low-density voids are ionized last and hence contain the hottest gas at the end of reionization, which leads to an at least partially inverted temperature–density relation of the IGM (Furlanetto & Oh 2009; Lidz & Malloy 2014; D’Aloisio et al. 2015, 2019). Oñorbe et al. (2019) modeled this process in detail, and their model (see Section 4.2) has an average slope of

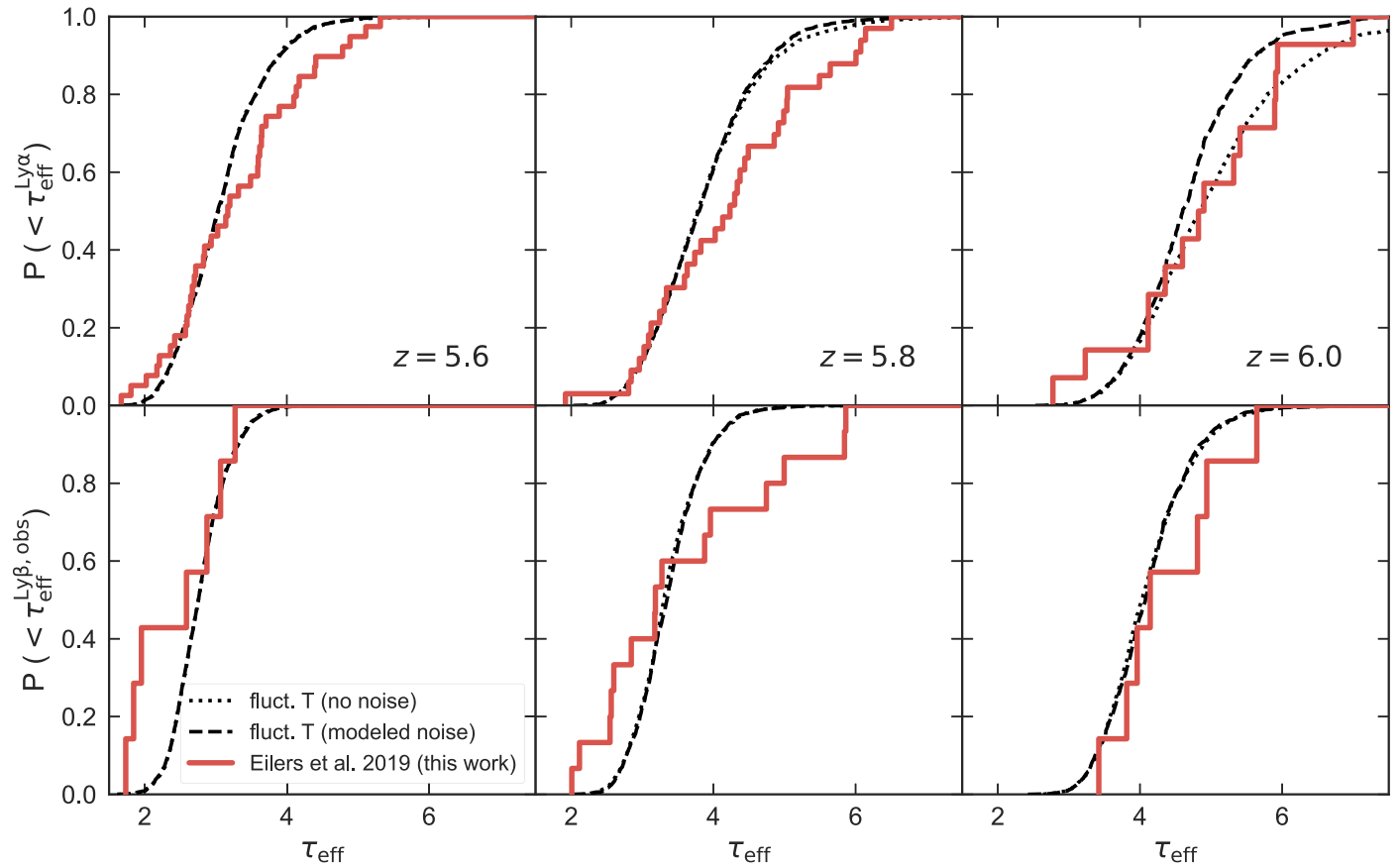


Figure 6. Same as Figure 5, for the reionization model with a fluctuating temperature field.

the temperature–density relation of  $\gamma \approx 1.1$ , i.e., roughly isothermal, at  $z \sim 6$ , but with a very large scatter (see their Figure 5), which arises due to a superposition of different heat injections and subsequent cooling at different times. Thus, their model predicts that at least some regions of the IGM do indeed follow an inverted temperature–density relation. This could explain why the model with a fluctuating temperature field (Figure 6) matches the  $\tau_{\text{eff}}^{\text{Ly}\alpha, \text{obs}}$  observations better than the model with fluctuations in the UVB (Figure 5).

Although Furlanetto & Oh (2009) claim that rapid adiabatic and Compton cooling will quickly erase any inversion of the thermal state of the IGM after the reionization event, we might still be observing the end stages of this process at  $z \sim 5.5$ – $6.0$ . This result complies with the conclusions from Trac et al. (2008). Contrary to Furlanetto & Oh (2009), they argue that the inversion of the IGM endures long past the reionization process (see also Finlator et al. 2018). Thus, our results provide support for a late and extended EoR, which is also in good agreement with several recent studies (Bosman et al. 2018; Eilers et al. 2018; Planck Collaboration et al. 2018; Kulkarni et al. 2019).

### 5.3. Evidence for Stronger Fluctuations in the Opacity of the Ly $\alpha$ Forest

In previous studies, comparisons of  $\tau_{\text{eff}}$  measurements to reionization models have been performed assuming an infinite S/N ratio of the simulated skewers. These noise-free predictions for the CDFs of  $\tau_{\text{eff}}$  correspond to the dotted curves in Figures 5–7. However, in order to conduct a proper comparison between the noisy data of any realistic data set to these models,

it necessary to model the spectral noise. Thus, as discussed in Section 4.5, we forward model our observations by adding spectral noise to the simulated skewers.

The models including the forward-modeled noise are shown as the dashed curves in Figures 5–7, which predict less scatter at high optical depths. As a result, the models with a spatially inhomogeneous reionization process that had been claimed previously to fully reproduce the scatter in the Ly $\alpha$  opacity observations (Figures 5 and 6) do *not* contain enough spatial fluctuations once we account for the spectral noise in the data. This discrepancy is most obvious in the top right panel of each figure for  $\tau_{\text{eff}}^{\text{Ly}\alpha}$  measurements at  $z = 6.0$ .

The reason for this discrepancy is quite simple: In any realistic data set, there will be a distribution in the S/N ratios of the spectra due to the various object magnitudes and exposure times. This noise manifests as noisy  $\tau_{\text{eff}}$  measurements. In order to detect a very high  $\tau_{\text{eff}}$ , one must not only encounter a rare fluctuation in the IGM along a quasar sightline, but this fluctuation must also be probed by a sufficiently bright quasar or deep enough spectrum to measure a high  $\tau_{\text{eff}}$ . Thus, large  $\tau_{\text{eff}}$  fluctuations in the IGM need to be more common than one naively expects from infinite S/N models.

We conclude that the forward modeling of spectral noise is essential to conduct a fair data model comparison, and our results suggest that stronger spatial inhomogeneities than previously assumed are needed to fully capture the observations. At lower opacities, the difference between perfect and noisy models is less significant, as most measurements are actually high-S/N detections rather than lower limits.

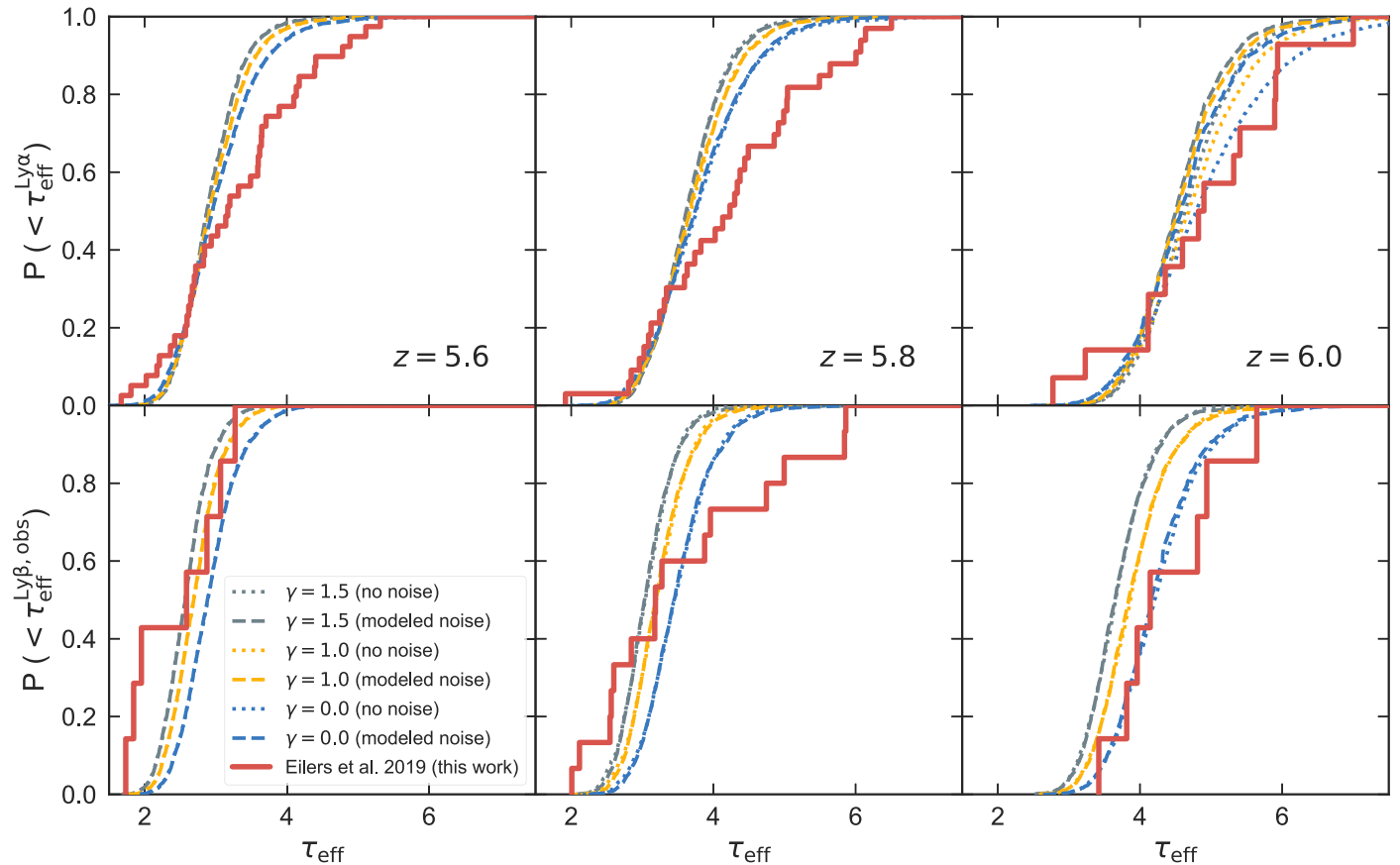


**Figure 7.** Same as Figure 5 for the reionization model with a uniform UVB but different slopes of the temperature–density relation of the IGM.

## 6. Summary

In this paper, we measured the IGM opacity in the  $\text{Ly}\alpha$  as well as the  $\text{Ly}\beta$  forest along 19 quasar sightlines. Due to the different oscillator strengths of their transitions, the  $\text{Ly}\alpha$  and  $\text{Ly}\beta$  optical depth depend on different gas densities, temperatures, and photoionization rates. Thus, the relation between  $\text{Ly}\alpha$  and  $\text{Ly}\beta$  optical depths provides new stringent constraints on the ionization and thermal state of the post-reionization IGM. A comparison of our measurements to several reionization models, which we obtain by post-processing the state-of-the-art *Nyx* hydrodynamical simulation, reveals two main results:

1. It is essential to account for the spectral noise in the data in order to conduct a fair comparison between the simulations and the observations. When forward modeling the spectral noise to the simulated skewers, the sensitivity to high-opacity regions becomes reduced. This arises from the fact that, in order to measure a high-opacity region in the universe along a quasar sightline, a high-quality spectrum of this quasar is required with a high S/N. Otherwise, a lower limit on the mean flux is adopted. Thus, in a realistic data set with different S/N ratios due to different exposure times and quasar luminosities, the sensitivity to high-opacity regions is lower than in models with infinite S/N skewers. Hence, forward modeling the noise to the simulations effectively decreases the scatter in optical depths predicted by the simulations. Thus, inhomogeneous reionization models including spatial UVB fluctuations or a

fluctuating temperature field, which have been believed to fully reproduce the  $\tau_{\text{eff}}^{\text{Ly}\alpha}$  measurements in previous studies, do not predict enough scatter between different quasar sightlines to match our observations. Hence, our results provide evidence for stronger spatial fluctuations in the reionization models to fully capture the observations than all previous studies assumed.

2. All current reionization models underpredict the opacity in the  $\text{Ly}\beta$  forest, when fine-tuning them to match the observations in the  $\text{Ly}\alpha$  forest. The difference increases with increasing redshift, when approaching the EoR. Models with a fluctuating temperature field seem to match the  $\text{Ly}\beta$  optical depths better than models with a fluctuations in the UVB, but it may require an even more inverted temperature–density relation of the IGM to fully capture the observed ratio of  $\text{Ly}\alpha$  and  $\text{Ly}\beta$  opacities at  $z \sim 6$ .

It remains to be seen whether the stronger spatial fluctuations required to match the observed opacities in the  $\text{Ly}\alpha$  forest would produce models that also match the as-yet under-predicted  $\text{Ly}\beta$  optical depths. If temperature fluctuations dominate and are stronger than current simulations suggest, then this could result in an IGM with an inverted temperature–density relation that might make the models more consistent with our measurements. Future models that encompass effects of fluctuations in the UVB as well as the temperature field (see discussion in Oñorbe et al. (2019)) could account for the fact that the reionization process ended relatively late (e.g., Kulkarni et al. 2019). It is not yet obvious how the interplay

between these various effects will change the predictions for the Ly $\alpha$  as well as the Ly $\beta$  optical depths. Thus, further modeling will be required to explain the observed opacity both in the Ly $\alpha$  as well as the Ly $\beta$  forest, which will hopefully lead to new insights regarding the morphology, timing, and thermal evolution of the reionization process.

The authors would like to thank the referee for very helpful and constructive feedback, which significantly improved our manuscript. Furthermore, we thank George Becker for sharing a few quasar spectra for a data comparison, as well as Vikram Khaira and Girish Kulkarni for helpful feedback and discussion.

The data presented in this paper were obtained at the W.M. Keck Observatory, which is operated as a scientific partnership among the California Institute of Technology, the University of California and the National Aeronautics and Space Administration. The Observatory was made possible by the generous financial support of the W.M. Keck Foundation.

This research has made use of the Keck Observatory Archive (KOA), which is operated by the W. M. Keck Observatory and the NASA Exoplanet Science Institute (NExScI), under contract with the National Aeronautics and Space Administration.

The authors wish to recognize and acknowledge the very significant cultural role and reverence that the summit of Maunakea has always had within the indigenous Hawaiian community. We are most fortunate to have the opportunity to conduct observations from this mountain.

Calculations presented in this paper used the hydra and draco clusters of the Max Planck Computing and Data Facility (MPCDF; formerly known as RZG). MPCDF is a competence center of the Max Planck Society located in Garching (Germany).

This work used the DiRAC Durham facility managed by the Institute for Computational Cosmology on behalf of the STFC DiRAC HPC Facility ([www.dirac.ac.uk](http://www.dirac.ac.uk)). The equipment was

funded by BEIS capital funding via STFC capital grants ST/P002293/1, ST/R002371/1 and ST/S002502/1, Durham University and STFC operations grant ST/R000832/1. DiRAC is part of the National e-Infrastructure.

*Software:* ESIRedux,<sup>9</sup> XIDL,<sup>10</sup> igmspec,<sup>11</sup> numpy (van der Walt et al. 2011), scipy (Jones et al. 2001), matplotlib (Hunter 2007), astropy (The Astropy Collaboration et al. 2018).

## Appendix A Matching the Quasar Spectra to Photometry Measurements

In order to avoid biases in the optical depths measurements due to potential issues in the quasar spectra that could have been introduced in the fluxing or coadding process, we verify that our final spectra match the observed photometric measurements in the  $i$ - and  $z$ -bands at central wavelengths of 7480 Å and 8932 Å, respectively. Thus, we integrate the observed flux underneath the filter curves and compare these integrated magnitudes to the photometry. To avoid contamination due to spurious negative pixels, we clip all pixels that are lower than  $2\sigma$ .

If necessary, we conduct a power-law correction to the quasar spectra:

$$f_{\lambda,\text{new}} = f_{\lambda} \cdot A \cdot \left( \frac{\lambda}{8932 \text{ Å}} \right)^{\alpha}, \quad (9)$$

by first calculating the amplitude  $A$  by matching the  $z$ -band photometry, and afterward estimating the slope  $\alpha$  by requiring the  $i$ -band magnitudes to match as well. The boundaries for both  $A$  and  $\alpha$  were set to  $[-3, 3]$ . A few examples are shown in Figure 8.

<sup>9</sup> <http://www2.keck.hawaii.edu/inst/esi/ESIRedux/>

<sup>10</sup> <http://www.ucolick.org/~xavier/IDL/>

<sup>11</sup> <http://specdb.readthedocs.io/en/latest/igmspec.html>



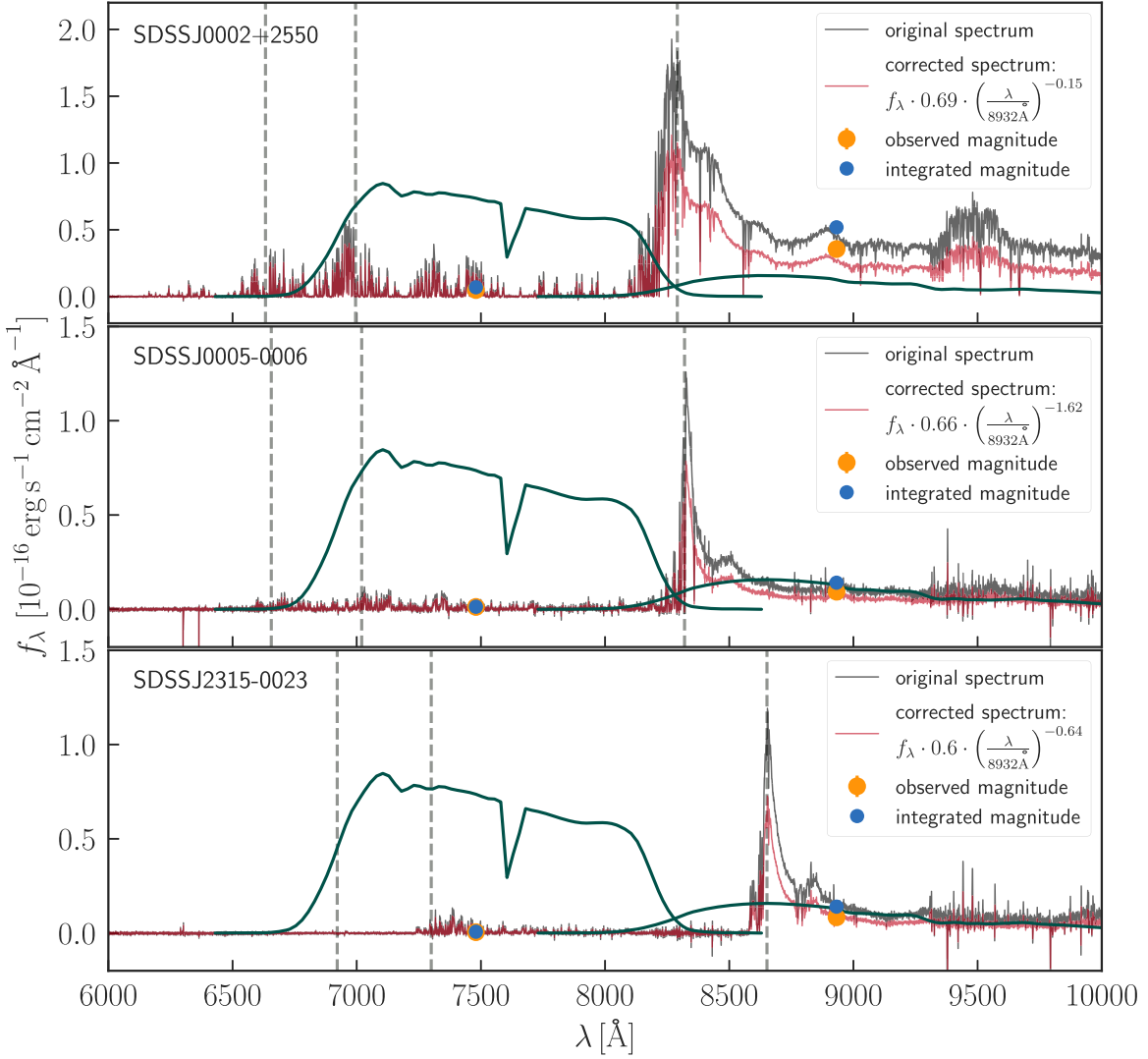


**Figure 8.** Three examples of our slightly corrected spectra (red) once they are matched to the observed photometry (orange data point) in the  $i$ - and  $z$ -bands. The original spectra are shown in black and the blue data points show the magnitudes in the  $i$ - and  $z$ -bands from the original flux integrated underneath the SDSS filter curves (dark green).

## Appendix B Additional Figures and Tables

We show the remaining  $\text{Ly}\alpha$  optical depth measurements for all 40 cMpc bins that do not have a  $\text{Ly}\beta$  forest measurement at the same absorption redshift  $z_{\text{abs}}$  in Table 3.

Figures 9 and 10 show all spectral bins for which we have both measurements of  $\tau_{\text{eff}}^{\text{Ly}\alpha}$  and  $\tau_{\text{eff}}^{\text{Ly}\beta, \text{obs}}$  around the same absorption redshift.

**Table 3**  
Remaining Mean Flux Measurements in the Ly $\alpha$  Forest

Object	$z_{\text{em}}$	$z_{\text{start}}$	$z_{\text{abs}}$	$z_{\text{end}}$	$\langle F^{\text{Ly}\alpha} \rangle$
SDSSJ0002+2550	5.82	5.528	5.486	5.445	$0.0269 \pm 0.0007$
		5.445	5.404	5.364	$0.0487 \pm 0.0007$
		5.364	5.324	5.284	$0.0195 \pm 0.0006$
		5.284	5.244	5.205	$0.0300 \pm 0.0005$
		5.205	5.166	5.128	$0.1421 \pm 0.0007$
		5.128	5.090	5.053	$0.0960 \pm 0.0008$
		5.053	5.015	4.978	$0.1751 \pm 0.0009$
		4.905	4.869	4.834	$0.0387 \pm 0.0004$
SDSSJ0005-0006	5.844	5.588	5.545	5.504	$0.0591 \pm 0.0043$
		5.504	5.462	5.421	$0.0272 \pm 0.0046$
		5.421	5.380	5.340	$0.0615 \pm 0.0052$
		5.340	5.300	5.261	$0.1019 \pm 0.0037$
		5.261	5.221	5.183	$0.0398 \pm 0.0045$
		5.183	5.144	5.106	$0.0837 \pm 0.0046$
		5.106	5.068	5.031	$0.1883 \pm 0.0059$
		5.031	4.994	4.957	$0.1396 \pm 0.0063$
		4.957	4.920	4.884	$0.0889 \pm 0.0036$
		4.884	4.848	4.813	$0.1628 \pm 0.0022$
CFHQSJ0050+3445	6.253	5.948	5.902	5.857	$0.0395 \pm 0.0051$
		5.857	5.812	5.767	$0.0275 \pm 0.0055$
		5.767	5.723	5.680	$0.0456 \pm 0.0040$
		5.680	5.637	5.594	$0.0420 \pm 0.0035$
		5.594	5.551	5.509	$0.0762 \pm 0.0041$
		5.509	5.468	5.427	$0.1910 \pm 0.0036$
		5.427	5.386	5.346	$0.1997 \pm 0.0042$
		5.346	5.306	5.266	$0.0767 \pm 0.0030$
		5.266	5.227	5.188	$0.1952 \pm 0.0030$
SDSSJ0100+2802	6.3258	6.055	6.008	5.962	$0.0074 \pm 0.0005$
		5.962	5.916	5.871	$0.0027 \pm 0.0007$
		5.871	5.826	5.781	$0.0010 \pm 0.0007$
		5.781	5.737	5.693	$0.0023 \pm 0.0005$
		5.693	5.650	5.607	$0.0268 \pm 0.0004$
		5.607	5.565	5.523	$0.0745 \pm 0.0006$
		5.523	5.481	5.440	$0.0357 \pm 0.0005$
		5.440	5.399	5.358	$0.1558 \pm 0.0005$
		5.358	5.318	5.278	$0.1094 \pm 0.0005$
ULASJ0148+0600	5.98	5.666	5.623	5.580	$-0.0014 \pm 0.0025$
		5.580	5.538	5.496	$0.0204 \pm 0.0032$
		5.496	5.455	5.414	$0.0933 \pm 0.0030$
		5.414	5.373	5.333	$0.0640 \pm 0.0031$
		5.333	5.293	5.253	$0.0975 \pm 0.0020$
		5.253	5.214	5.175	$0.1768 \pm 0.0025$
		5.175	5.137	5.099	$0.1995 \pm 0.0026$
		5.099	5.061	5.024	$0.2439 \pm 0.0038$
		5.024	4.987	4.950	$0.1394 \pm 0.0029$
PSOJ036+03	6.5412	6.222	6.173	6.125	$-0.0003 \pm 0.0017$
		6.125	6.078	6.031	$-0.0024 \pm 0.0014$
		6.031	5.984	5.938	$-0.0024 \pm 0.0013$
		5.938	5.893	5.847	$-0.0023 \pm 0.0018$
		5.847	5.802	5.758	$0.0019 \pm 0.0012$
		5.758	5.714	5.671	$0.0073 \pm 0.0007$
		5.671	5.628	5.585	$0.0122 \pm 0.0009$
		5.585	5.542	5.501	$0.0942 \pm 0.0023$
		5.501	5.459	5.418	$0.0634 \pm 0.0021$
PSOJ060+25	6.18	5.879	5.834	5.789	$0.0163 \pm 0.0119$
		5.789	5.745	5.701	$0.0390 \pm 0.0071$

**Table 3**  
(Continued)

Object	$z_{\text{em}}$	$z_{\text{start}}$	$z_{\text{abs}}$	$z_{\text{end}}$	$\langle F^{\text{Ly}\alpha} \rangle$
SDSSJ0836+0054	5.81	5.701	5.658	5.615	$0.0041 \pm 0.0042$
		5.615	5.572	5.530	$0.1139 \pm 0.0050$
		5.530	5.488	5.447	$0.0321 \pm 0.0055$
		5.447	5.406	5.366	$0.0196 \pm 0.0046$
		5.366	5.326	5.286	$0.0721 \pm 0.0039$
		5.286	5.246	5.207	$0.0649 \pm 0.0037$
		5.207	5.168	5.130	$0.1850 \pm 0.0041$
SDSSJ0840+5624	5.8441	5.524	5.483	5.441	$0.1431 \pm 0.0006$
		5.441	5.400	5.360	$0.0754 \pm 0.0006$
		5.360	5.320	5.280	$0.0452 \pm 0.0005$
		5.280	5.240	5.201	$0.0909 \pm 0.0004$
		5.201	5.163	5.124	$0.1142 \pm 0.0006$
		5.124	5.086	5.049	$0.1535 \pm 0.0006$
		5.049	5.011	4.975	$0.1599 \pm 0.0007$
		4.975	4.938	4.902	$0.1314 \pm 0.0005$
		4.902	4.866	4.830	$0.2934 \pm 0.0005$
SDSSJ1030+0524	6.309	5.521	5.480	5.438	$0.0225 \pm 0.0018$
		5.438	5.397	5.357	$0.1171 \pm 0.0016$
		5.357	5.317	5.277	$0.0681 \pm 0.0013$
		5.277	5.237	5.198	$0.0683 \pm 0.0013$
		5.198	5.160	5.121	$0.1036 \pm 0.0016$
		5.121	5.083	5.046	$0.1209 \pm 0.0018$
		5.046	5.008	4.972	$0.1024 \pm 0.0021$
		4.972	4.935	4.899	$0.1521 \pm 0.0013$
		4.899	4.863	4.827	$0.1914 \pm 0.0010$
SDSSJ1137+3549	6.03	5.968	5.922	5.876	$0.0163 \pm 0.0037$
		5.876	5.831	5.787	$0.0440 \pm 0.0041$
		5.787	5.743	5.699	$0.0112 \pm 0.0022$
		5.699	5.655	5.612	$0.0262 \pm 0.0017$
		5.612	5.570	5.528	$0.1100 \pm 0.0025$
		5.528	5.486	5.445	$0.0822 \pm 0.0028$
		5.445	5.404	5.363	$0.1839 \pm 0.0028$
		5.363	5.323	5.283	$0.1393 \pm 0.0023$
		5.283	5.244	5.205	$0.1237 \pm 0.0016$
SDSSJ1148+5251	6.4189	5.697	5.653	5.610	$0.1641 \pm 0.0026$
		5.610	5.568	5.526	$0.0692 \pm 0.0031$
		5.526	5.484	5.443	$0.1263 \pm 0.0034$
		5.443	5.402	5.361	$0.1874 \pm 0.0033$
		5.361	5.321	5.281	$0.1294 \pm 0.0028$
		5.281	5.242	5.203	$0.2018 \pm 0.0025$
		5.203	5.164	5.126	$0.1494 \pm 0.0031$
		5.126	5.088	5.050	$0.0885 \pm 0.0038$
SDSSJ1306+0356	6.016	5.998	5.951	5.906	$0.0006 \pm 0.0005$
		5.906	5.860	5.815	$0.0022 \pm 0.0004$
		5.815	5.771	5.727	$0.0078 \pm 0.0003$
		5.727	5.683	5.640	$0.0160 \pm 0.0002$
		5.640	5.597	5.555	$0.0166 \pm 0.0003$
		5.555	5.513	5.471	$0.0154 \pm 0.0004$
		5.471	5.430	5.389	$0.0419 \pm 0.0004$
		5.389	5.349	5.309	$0.0566 \pm 0.0004$
SDSSJ1306+0356	6.016	5.709	5.665	5.622	$0.0673 \pm 0.0010$
		5.622	5.580	5.537	$0.0408 \pm 0.0013$
		5.537	5.495	5.454	$0.0347 \pm 0.0014$
		5.454	5.413	5.372	$0.0902 \pm 0.0013$
		5.372	5.332	5.292	$0.0666 \pm 0.0011$
		5.292	5.253	5.214	$0.0620 \pm 0.0010$

**Table 3**  
(Continued)

Object	$z_{\text{em}}$	$z_{\text{start}}$	$z_{\text{abs}}$	$z_{\text{end}}$	$\langle F^{\text{Ly}\alpha} \rangle$
ULASJ1319+0950	6.133	5.214	5.175	5.136	$0.1032 \pm 0.0011$
		5.136	5.098	5.060	$0.1284 \pm 0.0014$
		5.060	5.023	4.986	$0.0801 \pm 0.0015$
		5.841	5.796	5.752	$0.0354 \pm 0.0087$
		5.752	5.708	5.665	$0.0161 \pm 0.0040$
		5.665	5.622	5.579	$0.0432 \pm 0.0041$
		5.579	5.537	5.495	$0.0305 \pm 0.0054$
		5.495	5.454	5.413	$0.0852 \pm 0.0058$
		5.413	5.372	5.332	$0.0409 \pm 0.0049$
		5.332	5.292	5.252	$0.0580 \pm 0.0034$
SDSSJ1411+1217	5.904	5.252	5.213	5.174	$0.1965 \pm 0.0045$
		5.174	5.136	5.098	$0.1297 \pm 0.0045$
		5.618	5.575	5.533	$0.0274 \pm 0.0016$
		5.533	5.491	5.450	$0.0798 \pm 0.0019$
		5.450	5.409	5.368	$0.0684 \pm 0.0016$
		5.368	5.328	5.288	$0.0661 \pm 0.0014$
		5.288	5.249	5.210	$0.0453 \pm 0.0016$
		5.210	5.171	5.133	$0.1859 \pm 0.0017$
		5.133	5.095	5.057	$0.1225 \pm 0.0019$
		5.057	5.019	4.982	$0.1217 \pm 0.0024$
SDSSJ1602+4228	6.09	4.982	4.946	4.909	$-0.0032 \pm 0.0010$
		5.749	5.705	5.662	$0.0218 \pm 0.0021$
		5.662	5.619	5.576	$0.0583 \pm 0.0022$
		5.576	5.534	5.492	$0.0660 \pm 0.0024$
		5.492	5.451	5.410	$0.0441 \pm 0.0025$
		5.410	5.369	5.329	$0.0679 \pm 0.0025$
		5.329	5.289	5.249	$0.0633 \pm 0.0015$
		5.249	5.210	5.171	$0.1517 \pm 0.0019$
		5.171	5.133	5.095	$0.0625 \pm 0.0020$
		5.095	5.057	5.020	$0.1376 \pm 0.0027$

**Table 3**  
(Continued)

Object	$z_{\text{em}}$	$z_{\text{start}}$	$z_{\text{abs}}$	$z_{\text{end}}$	$\langle F^{\text{Ly}\alpha} \rangle$
SDSSJ1630+4012	6.065	5.763	5.719	5.675	$-0.0131 \pm 0.0033$
		5.675	5.632	5.589	$0.0041 \pm 0.0030$
		5.589	5.547	5.505	$0.0003 \pm 0.0038$
		5.505	5.463	5.422	$0.1239 \pm 0.0043$
		5.422	5.381	5.341	$0.0441 \pm 0.0046$
		5.341	5.301	5.262	$0.1392 \pm 0.0028$
		5.262	5.222	5.184	$0.0906 \pm 0.0037$
		5.184	5.145	5.107	$0.1107 \pm 0.0039$
		5.107	5.069	5.032	$0.1986 \pm 0.0048$
SDSSJ2054-0005	6.0391	5.765	5.721	5.678	$0.0179 \pm 0.0043$
		5.678	5.635	5.592	$0.0530 \pm 0.0045$
		5.592	5.549	5.507	$0.1882 \pm 0.0062$
		5.507	5.466	5.425	$0.1527 \pm 0.0062$
		5.425	5.384	5.344	$0.0782 \pm 0.0063$
		5.344	5.304	5.264	$0.1855 \pm 0.0042$
		5.264	5.225	5.186	$0.1197 \pm 0.0053$
		5.186	5.148	5.110	$0.2639 \pm 0.0067$
		5.110	5.072	5.034	$0.1857 \pm 0.0095$
SDSSJ2315-0023	6.117	5.740	5.696	5.653	$0.0261 \pm 0.0048$
		5.653	5.610	5.567	$0.0708 \pm 0.0058$
		5.567	5.525	5.483	$0.0276 \pm 0.0063$
		5.483	5.442	5.401	$0.0390 \pm 0.0067$
		5.401	5.360	5.320	$0.0762 \pm 0.0054$
		5.320	5.280	5.241	$0.1411 \pm 0.0044$
		5.241	5.202	5.163	$0.0920 \pm 0.0051$
		5.163	5.125	5.087	$0.2344 \pm 0.0045$

**Note.** The different rows show the name of the object and its emission redshift  $z_{\text{em}}$ , the start of the redshift bin  $z_{\text{start}}$ , the mean redshift of each bin  $z_{\text{abs}}$ , and the end of each bin  $z_{\text{end}}$ , as well as the measured mean flux of the continuum normalized spectra in the  $\text{Ly}\alpha$  forest.

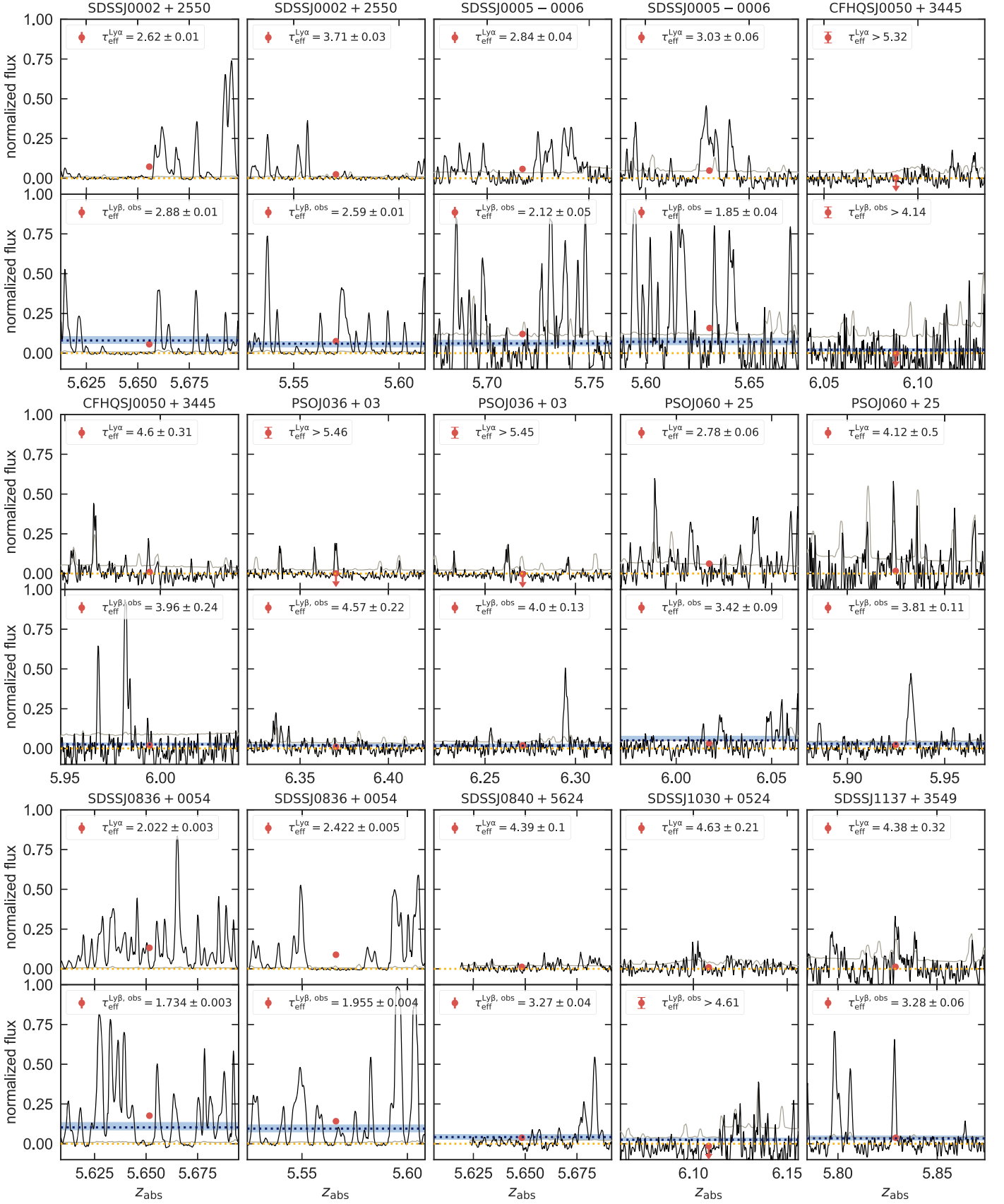


Figure 9. Same as Figure 2, for the remaining spectral bins.



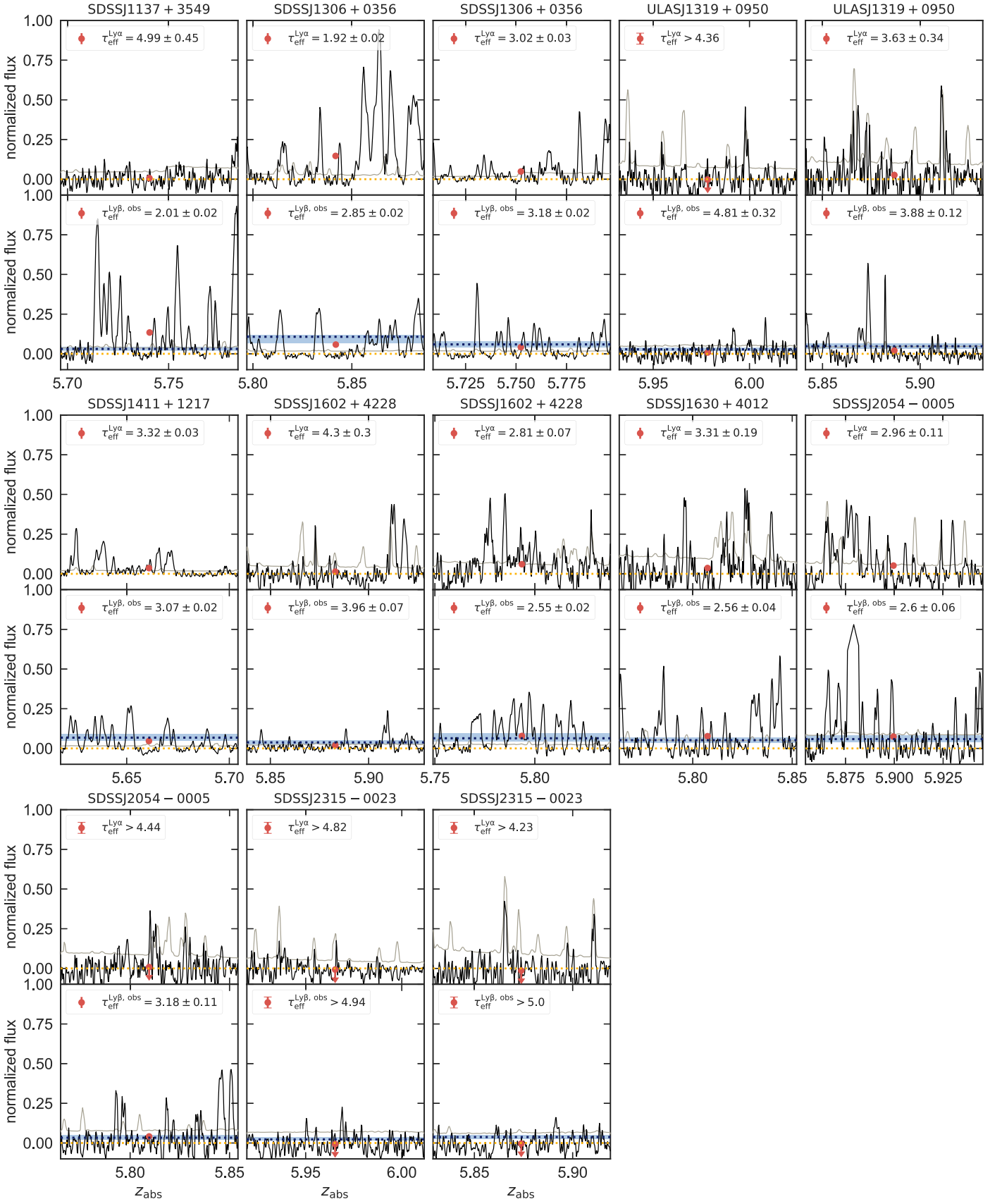
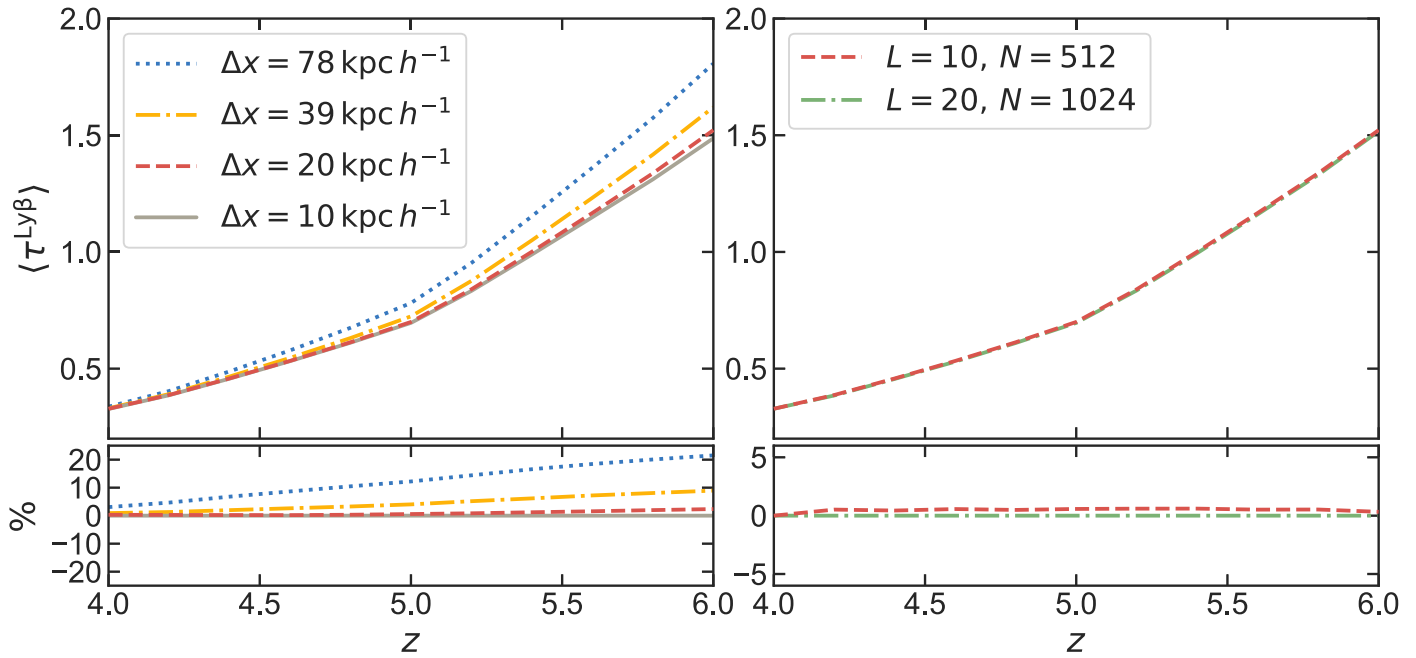


Figure 10. Same as Figure 2 and Figure 9.



**Figure 11.** Convergence of the mean Ly $\beta$  optical depth  $\langle\tau^{\text{Ly}\beta}\rangle$  at  $4.0 \leq z \leq 6.0$ . Left panel: simulations with a fixed box size ( $L = 10 \text{ Mpc } h^{-1}$ ) and different spatial resolution, i.e.,  $\Delta x = 78 \text{ kpc } h^{-1}$  (blue dotted),  $39 \text{ kpc } h^{-1}$  (yellow dashed-dotted),  $20 \text{ kpc } h^{-1}$  (red dashed), and  $10 \text{ kpc } h^{-1}$  (gray). Right panel: simulations with a fixed spatial resolution ( $\Delta x \sim 20 \text{ kpc } h^{-1}$ ) and different box sizes, i.e.,  $L = 10 \text{ Mpc } h^{-1}$  (red dashed),  $20 \text{ Mpc } h^{-1}$  (green dashed-dotted).

### Appendix C

#### Numerical Convergence of the Hydrodynamical Simulation

In this section, we discuss the numerical convergence of the the Ly $\beta$  forest in the N $\times$  hydrodynamical simulation. While several studies have shown the convergence of different Ly $\alpha$  forest statistics (e.g., Figure 6 in Oñorbe et al. (2017b); see also Bolton et al. (2017)), there has not been any convergence test on the Ly $\beta$  forest. We present here a first study on the Ly $\beta$  convergence making use of a publicly available suite of more than 60 N $\times$  hydrodynamical simulations.<sup>12</sup> We select several simulations from this suite in which we only changed the spatial resolution or the box size. Thus, all simulations use exactly the same photoionization rates at all redshifts.

We compute the Ly $\beta$  mean optical depth evolution directly from the simulated mean flux using Equation (4), without any rescaling of the photoionization rate. Convergence tests for the high- $z$  Ly $\alpha$  forest using the same suite of simulations can be found in Oñorbe et al. (2017b), and we refer the reader to their work for further details on the simulations. The left panel of Figure 11 shows the evolution of the mean Ly $\beta$  optical depth for four simulations with the same box size, i.e.,  $L = 10 \text{ Mpc } h^{-1}$ , but increasing numbers of resolution elements:  $128^3$  (blue dashed),  $256^3$  (yellow dashed-dotted),  $512^3$  (red dashed), and  $1024^3$  (gray), which results in cell sizes of  $\Delta x = 78, 39, 20$ , and  $10 \text{ kpc } h^{-1}$ , respectively. The  $512^3$  run has the same spatial resolution as the models discussed in this work (see Section 4). The right panel shows the convergence for different box sizes, i.e.,  $L = 10 \text{ Mpc } h^{-1}$  and  $20 \text{ Mpc } h^{-1}$ , at the same spatial resolution ( $\Delta x = 20 \text{ kpc } h^{-1}$ ). The simulations discussed in this work (red dashed lines in both panels) show a good convergence level below  $<5\%$  between  $4 \leq z \leq 6$ , both in terms of spatial resolution as well as box size. Therefore, we do not expect the resolution and/or box size of

the simulations to have any significant effect on the main conclusions of this work.

#### ORCID iDs

Anna-Christina Eilers <https://orcid.org/0000-0003-2895-6218>  
 Joseph F. Hennawi <https://orcid.org/0000-0002-7054-4332>  
 Frederick B. Davies <https://orcid.org/0000-0003-0821-3644>  
 Jose Oñorbe <https://orcid.org/0000-0002-8723-1180>

#### References

- Almgren, A. S., Bell, J. B., Lijewski, M. J., Lukić, Z., & Van Andel, E. 2013, *ApJ*, **765**, 39  
 Barnett, R., Warren, S. J., Becker, G. D., et al. 2017, *A&A*, **601**, A16  
 Becker, G. D., Bolton, J. S., Madau, P., et al. 2015, *MNRAS*, **447**, 3402  
 Becker, G. D., Davies, F. B., Furlanetto, S. R., et al. 2018, *ApJ*, **863**, 92  
 Bolton, J. S., Puchwein, E., Sijacki, D., et al. 2017, *MNRAS*, **464**, 897  
 Bosman, S. E. I., Fan, X., Jiang, L., et al. 2018, *MNRAS*, **479**, 1055  
 Bouwens, R. J., Illingworth, G. D., Oesch, P. A., et al. 2015, *ApJ*, **803**, 34  
 Calverley, A. P., Becker, G. D., Haehnelt, M. G., & Bolton, J. S. 2011, *MNRAS*, **412**, 2543  
 Chardin, J., Haehnelt, M. G., Aubert, D., & Puchwein, E. 2015, *MNRAS*, **453**, 2943  
 Chardin, J., Puchwein, E., & Haehnelt, M. G. 2017, *MNRAS*, **465**, 3429  
 D'Aloisio, A., McQuinn, M., Davies, F. B., & Furlanetto, S. R. 2018, *MNRAS*, **473**, 560  
 D'Aloisio, A., McQuinn, M., Maupin, O., et al. 2019, *ApJ*, **874**, 154  
 D'Aloisio, A., McQuinn, M., & Trac, H. 2015, *ApJL*, **813**, L38  
 Davies, F. B., Becker, G. D., & Furlanetto, S. R. 2018a, *ApJ*, **860**, 155  
 Davies, F. B., & Furlanetto, S. R. 2016, *MNRAS*, **460**, 1328  
 Davies, F. B., Hennawi, J. F., Eilers, A.-C., & Lukić, Z. 2018b, *ApJ*, **855**, 106  
 Dayal, P., & Ferrara, A. 2018, *PhR*, **780**, 1  
 Eilers, A.-C., Davies, F. B., Hennawi, J. F., et al. 2017a, *ApJ*, **840**, 24  
 Eilers, A.-C., Davies, F. B., & Hennawi, J. F. 2018, *ApJ*, **864**, 53  
 Eilers, A.-C., Hennawi, J. F., & Lee, K.-G. 2017b, *ApJ*, **844**, 136  
 Fan, X., Strauss, M. A., Becker, R. H., et al. 2006, *AJ*, **132**, 117  
 Faucher-Giguère, C.-A., Lidz, A., Hernquist, L., & Zaldarriaga, M. 2008a, *ApJL*, **682**, L9  
 Faucher-Giguère, C.-A., Prochaska, J. X., Lidz, A., Hernquist, L., & Zaldarriaga, M. 2008b, *ApJ*, **681**, 831

<sup>12</sup> THERMAL suite: <http://thermal.joseonorbe.com/>.

- Finlator, K., Keating, L., Oppenheimer, B. D., Davé, R., & Zackrisson, E. 2018, *MNRAS*, **480**, 2628
- Furlanetto, S. R., & Oh, S. P. 2009, *ApJ*, **701**, 94
- Haardt, F., & Madau, P. 2012, *ApJ*, **746**, 125
- Hui, L., & Gnedin, N. Y. 1997, *MNRAS*, **292**, 27
- Hunter, J. D. 2007, *CSE*, **9**, 90
- Jones, E., Oliphant, T., Peterson, P., et al. 2001, SciPy: Open Source Scientific Tools for Python, <http://www.scipy.org/>
- Keating, L. C., Puchwein, E., & Haehnelt, M. G. 2018, *MNRAS*, **477**, 5501
- Kulkarni, G., Keating, L. C., Haehnelt, M. G., et al. 2019, *MNRAS*, **485**, L24
- Lidz, A., Hui, L., Zaldarriaga, M., & Scoccimarro, R. 2002, *ApJ*, **579**, 491
- Lidz, A., & Malloy, M. 2014, *ApJ*, **788**, 175
- Lukić, Z., Stark, C. W., Nugent, P., et al. 2015, *MNRAS*, **446**, 3697
- McQuinn, M., & Upton Sanderbeck, P. R. 2016, *MNRAS*, **456**, 47
- Mesinger, A., & Furlanetto, S. 2007, *ApJ*, **669**, 663
- Mesinger, A., Furlanetto, S., & Cen, R. 2011, *MNRAS*, **411**, 955
- Oh, S. P., & Furlanetto, S. R. 2005, *ApJL*, **620**, L9
- Oñorbe, J., Davies, F. B., Lukić, Z., Hennawi, J. F., & Sorini, D. 2019, *MNRAS*, **486**, 4075
- Oñorbe, J., Hennawi, J. F., & Lukić, Z. 2017a, *ApJ*, **837**, 106
- Oñorbe, J., Hennawi, J. F., Lukić, Z., & Walthers, M. 2017b, *ApJ*, **847**, 63
- Pâris, I., Petitjean, P., Rollinde, E., et al. 2011, *A&A*, **530**, A50
- Planck Collaboration, Aghanim, N., Akrami, Y., et al. 2018, arXiv:1807.06209
- Prochaska, J. X. 2017, *A&C*, **19**, 27
- Sheinis, A. I., Bolte, M., Epps, H. W., et al. 2002, *PASP*, **114**, 851
- Shull, J. M., Stevans, M., & Danforth, C. W. 2012, *ApJ*, **752**, 162
- Songaila, A. 2004, *AJ*, **127**, 2598
- Suzuki, N. 2006, *ApJS*, **163**, 110
- Suzuki, N., Tytler, D., Kirkman, D., O'Meara, J. M., & Lubin, D. 2005, *ApJ*, **618**, 592
- Tang, J.-J., Goto, T., Ohyama, Y., et al. 2017, *MNRAS*, **466**, 4568
- The Astropy Collaboration, Price-Whelan, A. M., Sipőcz, B. M., et al. 2018, arXiv:1801.02634
- Trac, H., Cen, R., & Loeb, A. 2008, *ApJL*, **689**, L81
- Upton Sanderbeck, P. R., D'Aloisio, A., & McQuinn, M. J. 2016, *MNRAS*, **460**, 1885
- Vale, A., & Ostriker, J. P. 2004, *MNRAS*, **353**, 189
- van der Walt, S., Colbert, S. C., & Varoquaux, G. 2011, *CSE*, **13**, 22
- Wiese, W. L., & Fuhr, J. R. 2009, *JPCRD*, **38**, 565
- Willott, C. J., Delorme, P., Omont, A., et al. 2007, *AJ*, **134**, 2435
- Wyithe, J. S. B., & Bolton, J. S. 2011, *MNRAS*, **412**, 1926
- Zel'dovich, Y. B. 1970, *A&A*, **5**, 84